Université de Montréal

Modeling and Numerical Simulation of the clot detachment from a blood vessel wall

par

Sara Golyari

Département de mathématiques et de statistique
Faculté des arts et des sciences

Mémoire présenté à la Faculté des études supérieures
en vue de l'obtention du grade de
Maître ès sciences (M.Sc.)
en mathématiques

9 janvier 2018

SUMMARY

In this thesis we propose a model to numerically study the behavior of blood, which is considered as an incompressible Newtonian fluid, in the presence of a clot attached to a vessel wall. The purpose of this study is to find out whether different flow regimes may cause a clot to detach from a vessel wall or it would lead to a stable state. In Chapter 1, we give a literature review of previous studies modeling blood coagulation, blood clots in the vascular system, platelet adhesion and aggregation and pathological clot formation. Our work is mainly based upon some part of the mathematical model given by Bajd and Serša [3], which is presented in Chapter 1. Then, we will describe the mathematical modeling of the fluid representing the blood and the solid representing the clot in Chapter 2. The third chapter will focus on the numerical approach consisting of a projection method and the immersed boundary method [36] for solving the Navier-Stokes equations. Finally, in Chapter 4, we will discuss the results and give conclusions about the influence of different flow regimes on the clot stability.

Keywords : Blood coagulation, the Navier-Stokes equations, projection method, the immersed boundary method

SOMMAIRE

Dans ce mémoire, nous proposons un modèle pour étudier numériquement le comportement du sang, qui est considéré comme un fluide newtonien incompressible, en présence d'un caillot attaché à une paroi vasculaire. Le but de cette étude est de savoir si des régimes d'écoulement différents peuvent provoquer la décollement d'un caillot d'un mur de vaisseau ou conduire à un état stable. Dans le Chapitre 1, nous donnons une revue de la littérature sur les études précédentes, la modélisation de la coagulation sanguine, des caillots sanguins dans le système vasculaire, l'adhésion plaquettaire et l'agrégation et la formation de caillots pathologiques. Notre travail repose principalement sur une partie du modèle mathématique donné par Bajd et Serša [3], qui est présenté dans le chapitre 1. Ensuite, nous décrirons la modélisation mathématique du fluide représentant le sang et le solide représentant le caillot au chapitre 2. Le troisième chapitre se concentrera sur l'approche numérique consistant en une méthode de projection et la méthode de limite immergée [36] pour résoudre les équations de Navier-Stokes. Enfin, au Chapitre 4, nous discuterons des résultats et donnerons des conclusions sur l'influence de différents régimes d'écoulement sur la stabilité du caillot.

Mots-clés : la coagulation du caillot, les équations de Navier-Stokes, la méthode de projection, la méthode des frontières immergées

CONTENTS

LIST OF TABLES

LIST OF FIGURES

DEDICATIONS

To my parents and to Olivier Essiminy.

ACKNOWLEDGMENTS

First I would like to thank my supervisor Robert G. Owens, whose constant support, point of views and thoughtful suggestions were always encouraging and enriched the quality of this thesis.

I would like to thank the staff of the Department of Mathematics and Statistics for being helpful and supportive and a special thank to Anne-Marie Dupuis (TGDE) Michele Nasoni (IT manager) for being very professional, helpful, passionate and patient.

I am very grateful of having had the chance to find some of my best friends in this department, who have been always encouraging and supportive. Special thanks to my friends Masoume and Cintia who have been always supporting me and I could count on them at any time.

I would like to thank my friends Golsa and Mahmoud, who are always a great help and support, specially on the first days after my arrival to Canada

I am sincerely honoured of being accompanied by my best friend and my life partner Olivier Essiminy, who has been a truely positive support to accomplish my thesis.

I am highly thankful to my parents, whose unconditional love and support are indescribable. I would like also to thank my brothers, Kaveh and Keyhan, for everything that they have done for me.

Chapter 1

INTRODUCTION

Hemostasis is a process causing bleeding to stop, meaning that within a damaged blood vessel it is the first stage in wound healing. This involves blood changing from a liquid to a gel. The intact blood vessels play a central role in moderating blood's tendency to clot. When endothelial injury occurs, the endothelial cells stop secretion of coagulation and aggregation inhibitors. Therefore, three steps are included in hemostasis:

1. vasoconstriction (blood vessels narrowed as a result of contraction),

2. temporary blockage of a wound by a platelet plug,

3. blood coagulation (formation of a fibrin clot).

Blood coagulation is a mechanism by which the blood changes from a liquid to a gel and involves the activation, adhesion and aggregation of platelets along with deposition and maturation of fibrin - a participating protein in blood clotting. Thrombosis is the result of a blood clot inside a blood vessel obstructing the flow of blood through the circulating system. Blood platelets take part in both hemostasis and thrombosis. Disorders of coagulation are disease states which can result in hemorrhage (bleeding) or thrombosis. In 1966, Levin [26] proposed a linear mathematical model of coagulation kinetics. Since then, several non-linear models have been reported [21, 23, 37, 42, 47]. Thrombogenicity refers to the tendency of a material in contact with the blood to produce a thrombus (clot). It not only refers to fixed thrombi but also to emboli, clots which have become detached and travel through the blood stream. All materials are considered to be thrombogenic with the exception of the normal state of endothelial cells which line blood vessels.

Blood coagulation can also occur because of some pathological diseases, such as arteriosclerosis (the thickened and less elastic walls of arteries (blood vessels that carry blood away from the heart)), one of many lifestyle diseases. In such situations, coagulation is initiated without wall injury. In contrast, thrombolysis (blood clot dissolution) has led to clinical approaches for the

restoration of vessel patency after a partial or complete blood-flow obstruction in massive thrombosis. As a measure of the importance of this procedure, researchers have tried to construct and to propose mathematical models describing thrombolysis.

1.1. THROMBOSIS AND COAGULATION

Thrombosis is an extremely complex dynamic process that involves many disparate types of mechanical, biophysical, biochemical, cell activation and polymerization interactions [16].

The primary obstacles to turning the thrombin (an enzyme catalyzing coagulation reactions) production on are physical (flow and platelet deposition) not chemical inhibitors. Transport within the growing thrombus may be very important in determining the eventual size and structure of the thrombus.

The interplay between physical and chemical processes is critical to understanding thrombosis. Mathematical modeling and computational simulations are essential tools in comprehending this interplay and the function of the clotting system as an integrated dynamical system.

Experimental studies have recognized that clot formation rarely occurs in regions of parallel flow, but primarily in regions of stagnation point flows, within blood vessel bifurcation, branching and curvature. Following a vessel wall disruption, an immediate reaction is triggered that promotes vasoconstriction , i.e. minimizing vessel diameter and diminishing blood loss. During activation, platelets undergo intrinsic and extrinsic mechanisms leading to a series of chemical and morphological changes. The platelet starts balling up into a spherical shape and extends a number of appendages called pseudopodia. It leads to a sufficiently flexible structure that over time can spread out over the surface to which it adhered. Organelles (specialized subunits within the platelet) in the platelet's cytoplasm bind to collagen (exposed by arterial damage) and release their contents of cytoplasmic granules containing chemicals like adenosine diphosphate (ADP) and platelet-activating factors. Other platelets attracted by ADP are activated, interact with plasma proteins like fibrin and fibrinogen (a protein produced by the liver which helps stop bleeding) and promote platelet aggregation and adhesion to sub-endothelial tissue. This results in the formation of hemostatic plugs and is the primary step in hemostasis. However, it is observed that when the concentration of activators exceeds a threshold value, platelet aggregates resulting from this process can break up and cause aggregation at locations other than the site of damage.

1.1.1. Mathematical models

Bodnar and Sequeira [5] discussed a numerical simulation of the coagulation dynamics of blood. An incompressible generalized Newtonian model with shear-thinning viscosity was adopted to

describe the blood flow. Therefore, the application of the physical principles of momentum and mass conservation leads to the equations defined in the flow domain Ω

$$\rho\left(\frac{\partial \boldsymbol{u}}{\partial t} + \boldsymbol{u}.\nabla\boldsymbol{u}\right) = -\nabla p + \nabla.\boldsymbol{\tau}(\boldsymbol{u}),$$
$$\nabla.\boldsymbol{u} = 0,$$

where $\boldsymbol{u}(t,x)$ and $p(t,x)$ are the blood velocity and the pressure defined in Ω, the vascular lumen, for $t \geq 0$. The equation is completed with appropriate initial and boundary conditions. ρ is the fluid density and $\boldsymbol{\tau}(\boldsymbol{u})$ is the deviatoric stress tensor, proportional to the symmetric part of the velocity gradient, given by

$$\boldsymbol{\tau}(\boldsymbol{u}) = 2\mu(\dot{\gamma})\boldsymbol{D},$$

such that

$$\boldsymbol{D} = \frac{1}{2}(\nabla\boldsymbol{u} + \nabla\boldsymbol{u}^T)$$

is the stretching tensor, $\dot{\gamma}$ is the shear rate and $\mu(\dot{\gamma})$ is the shear-rate dependent viscosity function which decreases with increasing shear rate.

Advection-diffusion-reaction equations modeling the cascade of biochemical reactions included in the coagulation process described the evolution in time and space of various enzymes and zymogenes, proteins, inhibitors, tissue pathway plasminogen activator and fibrin/fibrinogen involved in the extrinsic pathway of the blood coagulation and fibrinolysis (a process that prevents the problematic growth of the blood clot) in quiescent plasma. Zymogenes are inactive enzyme precursors and plasminogen is a glycoprotein circulating in the blood and is the precursor of plasmin, an important enzyme which degrades many plasma proteins. A tissue pathway plasminogen activator is an enzyme converting fibrin/fibrinogen involved in the extrinsic pathway of the blood coagulation. These equations are expressed as:

$$\frac{\partial C_i}{\partial t} + \Delta.(C_i\boldsymbol{u}) = \nabla.(D_i\boldsymbol{\nabla}C_i) + R_i,$$

where C_i stands for concentration of the *i*th reactant, D_i denotes the corresponding diffusion coefficient (which could be a function of the shear rate) and $\boldsymbol{u}$ is the velocity field. R_i is a nonlinear reaction term that represents the production or depletion of C_i due to an enzymatic cascade of reactions.

The authors obtained a numerical solution of the coupled fluid-biochemistry using a three-dimensional code based on a finite-volume semi-discretization in space, on structured grids, where both inviscid and viscous flux integrals were evaluated using centered cell numerical fluxes. An explicit multistep Runge-Kutta scheme was used for the time integration.

1.1.2. A mathematical model of a blood clot in the human vascular system

Appiah *et al.* [2] hypothesized that clot dynamics are proportional to the flow rate of blood plasma dissipated along the clot. Therefore, they studied the velocity of three different blood flow regimes. Turbulence can occur for de-accelerated flow during diastole (the period when the heart refills with blood after contraction) even at Reynolds numbers less than 1000. Electrographs of recanalisation channels (the reopening of previously blocked blood vessels) through blood clots showed that non-occlusive blood clots have rough walls and since flow along non-occlusive clots is pulsatile, the onset of turbulence is expected at Reynolds numbers lower than 2000. It was considered that there are three possible situations for the flow through the narrowed segment along the clot; i.e. laminar-laminar flow, laminar-turbulent flow and turbulent-turbulent flow (Figs. 1.1-1.2) For the first case,

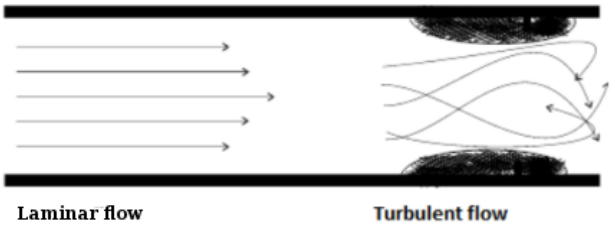

FIGURE 1.1. The material volume

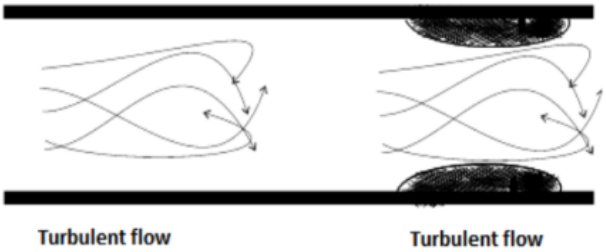

FIGURE 1.2. The material volume

the flow velocity was modeled as

$$\boldsymbol{v}_2 = \boldsymbol{v}_L \frac{1}{x + \frac{1}{Mx}},$$

where $\boldsymbol{v}_L$ and M are, respectively, the average blood velocity in the first vessel segment alone and the ratio between the length of the first segment (l_1) and that of the second vessel segment (l_2) defined to be the channel where the blood flows around a non-occlusive clot. x is the ratio between the cross sectional areas of the two vessel segments. In the second situation,

$$\boldsymbol{v}_2 = \boldsymbol{v}_{LT} M x^{3/2} \left(\sqrt{1 + \frac{N}{Mx^{5/2}}} - 1 \right),$$

where M has the same meaning as for the case of laminar- laminar flow; and

$$\boldsymbol{v}_{LT} = \frac{4\pi\eta}{f\rho\sqrt{A_1}} \quad \text{and} \quad N = \frac{f\rho\Delta p A_1^{3/2}}{16\pi^2\eta^2 l_1}.$$

A_1 is the cross sectional area of the first segment; Δp is the pressure drop, ρ is the density, f is a frictional coefficient and η is the fluid viscosity coefficient. Lastly, for the turbulent-turbulent case:

$$\boldsymbol{v}_2 = \boldsymbol{v}_t \frac{1}{\sqrt{x^2 + \frac{1}{M\sqrt{x}}}},$$

where $\boldsymbol{v}_T$ corresponds to the blood velocity when the clot is totally dissolved ($x = 1$).

The conclusion was that in the cases of both the laminar-laminar and the turbulent-turbulent cases the clot will not have any effect on the human system since the velocity and pressure of the blood keep decreasing as the ratio between the lengths and the ratio between the cross-sectional areas is increased. In the case of the laminar-turbulent flow since the velocity and pressure of the blood increase until they hit a maximum as M and x are increased the clot will have an effect on the human system. At the peak of the blood velocity this effect is high blood pressure.

In 2011, a mathematical model of the lysis (break down) of clots in blood vessels was constructed on the basis of the convection-diffusion equations by Khramchenkov and Khramchenkov [24]. The fibrin clot was considered as an immobile solid phase, and the plasminogen, plasmin, and plasminogen activators as dissolved liquid phases. As a result of the numerical solution of the model, predictions of the development of the lysis process have been obtained.

In critical situations caused by the clogging of important vessels with a clot, the necessity for dissolving the clot with the help of lytic means arises which dissolve fibrin. The physical and biochemical structures of the clot depend on many factors: the concentration of thrombin and fibrinogen, the ionic strengths in the solution, and hemodynamic forces.

The lysis process consists of the plasminogen–activator entering into a reaction with plasminogen to form the active substance plasmin. The latter reacts with fibrin fibers of the clot gradually destroying them and penetrating into the clot material under the action of the transfer and diffusion. The tissue plasminogen activator reacts with the plasminogen on the fibrin surface where it settles in the course of penetration into the fibrin structure.

The problem is that the process of transfer of lytic agents proceeds due to convection and diffusion. Convection in the clot is highly impeded, and diffusion is a comparatively long process. The process of plasminogen-to-plasmin transformation takes a few minutes, while penetration and destruction of even small clots requires about an hour or more. Thereafter, it is necessary to have as complete information on the dissolution dynamics and the character of motion of components of the lysis process as possible.

To obtain a mathematical model of the lysis of clots in the blood vessels, it is necessary to construct a system of equations of filtration in a deformable porous medium with a porous skeleton of variable mass. The mass of the porous skeleton substance was considered as:

$$M_s = (1-\varepsilon)\rho_s V_0 exp(\theta),$$

where V_0 is the initial value of the volume of the deformed porous medium, θ is the cubic expansion coefficient of the solid phase material and ρ_s is the density of the solid phase substance. The change in the clot porosity is described by the expression:

$$\frac{\partial \varepsilon}{\partial t} = (1-\varepsilon)\frac{\partial \theta}{\partial t} - \frac{2(1-\varepsilon)R_t'}{R_s},$$

and $R_t' = \frac{\partial R_s}{\partial t}$ and the equation of shrinkage of the clot skeleton is:

$$\frac{\partial \theta}{\partial t} + \frac{\partial v}{\partial x} = \frac{2(1-\varepsilon)R_t'}{R_s},$$

where R_s is the fibrin fiber radius, v is the current value of the deformed porous medium and ε is the porosity.

On the basis of the model a numerical scheme was constructed for investigating the processes in the course of dissolution of the clot. With the use of the developed model, the lysis dynamics, the motion of clot components in the blood plasma and fibrin, and the influence of the clot characteristics on the lysis process were investigated. The volume of the introduced lytic agents and the duration of their action depending on the rheological properties and deformations of the clot material have been determined. The results of this research led to prediction of the conditions for the development of thrombosis and thrombolysis in the human organism.

An injury of a blood vessel requires quick repair of the wound in order to prevent a loss of blood. This is done by a hemostatic system. The key point of the work of Tokarov et al. [**44**] was the formation of an aggregate of platelets. A mathematical model was proposed in which the movement of its boundary due to the adhesion and detachment of platelets was determined by the level set method. The model took into account the inhomogeneous distribution of erythrocytes (red blood cells) and platelets across the blood flow, the reversible adhesion of platelets, their activation, secretion, and aggregation. The calculation results were in accordance with the experimental data concerning the kinetics of the ADP-evoked growth of a thrombus in vivo for different flow velocities. Platelets are instantly activated near the injured vascular wall and become capable of strong adhesion to the wall and to each other. The platelet carried by the flow were captured at the rate

$$W_{RP}^{adh} = \alpha J_{RP}^{wall} \chi \frac{\Theta}{s},$$
$$W_{AP}^{adh} = \alpha J_{AP}^{wall} \chi \frac{\Theta}{s},$$

where α is the capture efficiency, J_{RP} and J_{AP} are the platelet flows toward the wall. The function Θ is the surface indicator (it is greater than zero in the transition zone where the adhesion occurs and is equal to zero outside it) and s is the width of the transition zone. The function χ indicates the ability of the surface of the aggregate on a vascular wall to fix a platelet.

They neglected the differences in the densities of erythrocytes and the plasma and the non-Newtonian properties of the blood because they become evident only for shear velocities $\sim 50s^{-1}$ and lower, whereas the typical shear velocities in microcirculation vessels are $0.5 \times 10^3 s^{-1}$. Therefore, the rate of convection of free erythrocytes and free platelets was assumed to be equal to the velocity of the medium. The platelets fixed in the aggregate were assumed to be motionless.

Tokarov *et al*. took into account only the basic soluble activators of platelets, ADP, because the other activators (thrombin and thromboxane A2 (a stimulating activator of new platelets as well as increasing platelet aggregation)) were considered similar to ADP.

The near-wall shear velocity was the main parameter determining the influence of the flow on the thrombocyte components of hemostasis, because it controls the delivery rate of platelets to the point of adhesion and their detachment by the flow and also the velocity of the convection drift of thrombocyte activators. So, they studied the influence of shear velocity on the thrombus growth rate in their model. An advantage of their model is its flexibility and its ability to be integrated into continuous models of blood flow in domains with a complete geometry and with fixed or moving walls, and also for the whole vascular network.

1.1.3. Mathematical models of Fogelson

1.1.3.1. *Studying platelet adhesion and aggregation*

In 1984, Fogelson et al. [13] studied platelet aggregation on a microscopic scale, representing blood by a viscous incompressible fluid in which discrete massless platelets are suspended. The diffusion-like motion of platelets which was observed experimentally in flowing blood was simulated and it was thought to result from local "stirring" induced by tumbling and colliding among the much larger red blood cells which occupy 45 percent of blood volume. This additional platelet motion is important, for it provides a mechanism for platelet transport to the vessel wall. They regarded platelets as point particles which can generate local forces and the geometry of the domain in which the equations of the model were solved remained constant in time. They expressed the transport of adenosine diphosphate (ADP) as the advection-diffusion equation:

$$\frac{\partial c}{\partial t} + \boldsymbol{u}.\boldsymbol{\nabla} c = \sigma \Delta c + s(s,t),$$

where $c(x,t)$ is the concentration of ADP, σ is the ADP diffusion coefficient, and $s(x,t)$ is the source term created by the release of ADP [13].

The model was restricted to two spatial dimensions to economize on computer and memory. The numerical method applied grid-based finite difference schemes to solve the fluid dynamics and ADP-transport equations. Deploying a simple Euler scheme, the platelets were tracked independently of the grid to solve for the advective motion. Moreover, a random walk technique was used to simulate the diffusive motion. To avoid large instabilities, an implicit scheme was used to determine the intra-platelet forces.

In 1992, Fogelson [14] developed continuum models of the platelet aggregation process. Continuum models are based upon the interactions in a viscous, incompressible fluid; a population of nonactivated and activated platelets; a distribution of interplatelet links, and an interplatelet signaling chemical. The two equations given below describe the assumption that nonactivated platelets are transported by convection and diffusion and that the transport of activated platelets by convection and their creation by the activation of non-activated platelets

$$\frac{\partial \phi_n}{\partial t} + \boldsymbol{u}.\nabla\phi_n = D_n \triangle \phi_n - R(c)\phi_n,$$
$$\frac{\partial \phi_a}{\partial t} + \boldsymbol{u}.\nabla\phi_a = R(c)\phi_n,$$

where ϕ_n is the concentration of nonactivated platelets, ϕ_a is the concentration of activated platelets, $\boldsymbol{u}$ is the velocity vector, D_n is the diffusion coefficient and $R(c)\phi_n$ is the rate of conversion to activated platelets.

Nevertheless, the influence of variable diffusion was not considered in this study. It was concluded that the presence of sufficient concentrations of activated platelets and interplatelet links within a portion of the suspending fluid can alter the behavior of the composite material from that of a viscous fluid to that of an elastic solid. In addition, Fogelson claimed that there exists an interesting possibility of a chemically-induced fluid-to-solid phase transition.

1.1.3.2. *Continuum models of platelet aggregation*

Later on, Fogelson [14] turned his attention to the development of continuum models of the platelet aggregation process. His model was appropriate for studying aggregation in the smallest arteries, which have a diameter of approximately $50\mu m$, but it was not suitable for studying aggregation in vessels the size of the coronary arteries (diameter $\approx 1mm$) in which the number of platelets is enormous.

In 1999, computational methods for continuum models were proposed [46] to study mathematical models of platelet aggregation [14] in vessels of the size of the cornary arteries or larger.

Developing numerical methods for studying, in two dimensions, the general form of aggregation models [46], the general form required solving a four-dimensional partial differential equation. The evolution of the density of interplatelet bonds was described as

$$E_t + \boldsymbol{u}.\boldsymbol{\nabla}_x E + (\boldsymbol{v}.\boldsymbol{\nabla}\boldsymbol{u}).\boldsymbol{\nabla}_{\boldsymbol{v}} E = \alpha(|\boldsymbol{v}|)\phi_a^2 - \beta(|\boldsymbol{v}|)E,$$

where E is a function of time t, the spatial coordinates, as well as a vector $\boldsymbol{v}$ that expresses the connection between two ends of an intra-platelet bond. E is advected at velocity $\boldsymbol{u}$ in physical space and at velocity $\boldsymbol{v}.\nabla$ in $\boldsymbol{v}$-space. $\nabla_{\boldsymbol{v}} E$ refers to the difference in velocity $\boldsymbol{u}$ at the two ends of an intraplatelet bond. The new bonds were created at the rate $\alpha(|\boldsymbol{v}|)\phi_a^2$, and $\beta(|\boldsymbol{v}|)E$ is the rate of breaking down of the existing bonds.

To simulate the behavior of Fogelson's continuum models of platelet aggregation a numerical method was applied whose components were multidimensional high resolution finite difference schemes for advective transport, alternating direction implicit method for diffusive transport, and a new hybrid finite-difference spectral method for the model's elastic link transport equation.

1.1.3.3. *The influence of flow-mediated transport on the initiation and inhibition of coagulation*

Fogelson and Tania [18] discussed the interactions among coagulation biochemistry, platelet deposition, activation and flow-mediated transport of platelets and coagulation proteins in response to vascular injury. They assumed that prothrombin (a glycoprotein in the blood plasma and an essential component of the blood clotting mechanism) and thrombin competed for binding sites on an activated platelet. Later on, it was assumed that there are separate binding sites on the platelet for prothrombin and thrombin [17]. When a prothrombin molecule bound to an activated platelet, the resulting thrombin molecule immediately was released into the plasma, where it became subject to inhibition by ATIII (antithrombine, which is a small protein molecule that inactivates several enzymes of the coagulation system) and to being carried away by the flow. They assumed it could also rebind to a thrombin-specific site on an activated platelet. Along with other assumptions, since the earlier model [18] made predictions that had been validated experimentally, it was a reasonable standard against which to assess the quality of the new model with separate prothrombin and thrombin binding sites [18]. At shear rates of 50 s^{-1} or more, flow-mediated removal of thrombin is, by far and away, the dominant inhibitor of thrombin activity in the reaction zone of model simulations.

1.1.3.4. *Cell-based approach*

Cell-based models were proposed for blood clotting [15] such that platelet aggregation formed during the blood clotting was modeled on two scales, microscopic and macroscopic. For the former, a

major tool is the immersed boundary (IB) method [34]. The fundamental problem for which the IB method had been developed concerns the interactions of a viscous incompressible fluid with one or more moving and/or deformable elastic objects in contact with that fluid. The immersed boundary force contributions are distributed to the Eulerian grid using a discrete version of following equation

$$\boldsymbol{f}(\boldsymbol{x},t) = \int \boldsymbol{F}(q,t)\delta(\boldsymbol{x} - \boldsymbol{X}(q,t))dq,$$

where $\boldsymbol{f}(\boldsymbol{x},t)$ represents the fluid force density in the terms of the boundary elastic force density $\boldsymbol{F}$, $\boldsymbol{x}$ is some point in the fluid, q is the elastic membrane parameter and $\boldsymbol{X}(q,t)$ is the position vector at time t of the membrane point labeled by q.

Each platelet and each vessel wall were represented as an IB object in this model, i.e., as a collection of elastically linked Lagrangian points so that each pair moved at the local fluid velocity. The model consists of stochastic and partial differential equations and auxiliary change of state conditions.

Each platelet was presented as a separate object using Peskin's IB method [34] in semi-discrete microscale models. Continuum macro-scale models were motivated by the IB idea of representing biological tissue as a compressible fluid-elastic material, so that changes in geometry or phase were manifested solely through changes in mechanical forces within the material. In addition, it was believed that the macroscale continuum models could be the basis of models of biological gels and their mechanics.

1.2. PATHOLOGICAL CLOT FORMATION

As mentioned before, there is a widespread concern regarding pathological clot formation which plays an important role in patients who suffer various diseases.

In 1998, a mathematical model for the prothrombin time test (a test to diagnose unexplained bleeding which studies the extrinsic and common pathways of the coagulation cascade and it is used to determine clotting tendency of blood) was proposed which anticipated that the test should be able to make known severe coagulation disorders connected with a more than five-fold decrease in the concentrations or activities of the blood coagulation factors. Pohl et al. [37] published a mathematical model of the extrinsic pathway in vitro (prothrombin time test) estimating unavailable kinetic constants by comparing the prothrombin time values in patients with the results of the mathematical modeling via a chi-square fit.

A tissue factor in vitro consists of a cascade of enzymatic reactions and three positive feedback loops [22]. According to Khanin et al. [22], a set of ordinary differential equations describing the balance for every component of the tissue factor pathway, such as a balance equation for factor Xa

maybe written as:

$$\begin{aligned}\frac{d[Xa]}{dt} =& \frac{K_{X,TF-VII}[X][TF-Vii]}{Km_{X,TF-VII}+[X]},\\ &+\frac{K_{X,TF-VIIa}[X][TF-VIIa]}{Km_{X,TF-VIIa}+[X]},\\ &+\frac{K_{X,VIIa}[X][VIIa]}{Km_{X,VIIa}+[X]} - K_{Xa-Va}[Xa-Va],\\ &-K_{ATIII-Xa}[ATIII][Xa] - K_{ATIII-[Xa-Va]}[ATIII][Xa-Va],\end{aligned}$$

where $K_{X,TF-VII}$, $K_{X,TF-VIIa}$ and $K_{X,VIIa}$ are direct measures of the catalytic production of product under optimum conditions (saturated enzyme) for corresponding enzymatic reactions. $Km_{X,TF-VII}$, $Km_{X,TF-VIIa}$ and $Km_{X,VIIa}$ are measures of the substrate concentration required for effective catalysis to occur) for these reactions. K_{Xa-Va}, $K_{ATIII-Xa}$ and $K_{ATIII-[Xa-Va]}$ are the second order constants for complex formation. $\frac{K_{X,TF-VII}[X][TF-Vii]}{Km_{X,TF-VII}+[X]}$ is factor X activation by tissue factor VIII complex. $\frac{K_{X,TF-VIIa}[X][TF-VIIa]}{Km_{X,TF-VIIa}+[X]}$ is the factor X activation by tissue factor VIIa complex; $\frac{K_{X,VIIa}[X][VIIa]}{Km_{X,VIIa}+[X]}$ is factor X activation by tissue factor VII. $K_{Xa-Va}[Xa-Va]$ is factor Xa decrease due to prothrombinase formation; $K_{ATIII-Xa}[ATIII][Xa]$ is the factor Xa decrease through the inhibition by ATIII; and lastly, $K_{ATIII-[Xa-Va]}[ATIII][Xa-Va]$ is factor Xa decrease through the inhibition of prothrombinase by ATIII (factors V, VII, X are some of the proteins in coagulation cascade; factor Va, VIIa, Xa are activated factors V, VII and X, respectively; tissue factor is a transmembrane receptor for Factor VII/VIIa (FVII/VIIa) prothrombinase complex catalyzes the conversion of prothrombin to thrombin).

It was known that the deficiency of coagulation factors may be connected not only with the decrease in their concentrations in plasma but also with the decrease in their enzymatic activities. The proposed mathematical model enabled the authors to obtain data which cannot be measured experimentally.

Another study done by Bajd and Serša [3] dealt with a coarse-grained molecular dynamics based microscale mathematical model of blood clot dissolution. In this model a blood clot was considered as "an assembly of blood cells interconnected with elastic fibrin bonds, which are cleaved either biochemically (bond degradation) or mechanically (bond overstretching) during flow-mediated thrombolysis". Thrombolysis is used in the treatment of ischemic cerebro-vascular stroke (a stroke caused by the interruption of blood flow to the brain owing to a blood clot) and pulmonary embolism (occurring when one or more arteries in the lungs becomes blocked) or as an auxiliary treatment in "acute arterial and deep-vein thrombosis" [10, 12, 32, 41]. The blood cell dynamics were calculated using Newton's second law. For a selected blood cell within a blood clot, the

equation of motion is therefore

$$m\boldsymbol{a}_i(t) = \sum_{j=1} \boldsymbol{F}^b_{i,j}(t) + \boldsymbol{F}^d_i(t) + \boldsymbol{F}^B_i(t) + \boldsymbol{F}^g_i + \boldsymbol{F}^{\bar{g}}_i,$$

where m is the mass of the blood cell, $\boldsymbol{a}_i(t)$ is the cell acceleration, $\boldsymbol{F}^b_{i,j}(t)$ is the binding force, $\boldsymbol{F}^d_i(t)$ is the net drag force, $\boldsymbol{F}^B_i(t)$ is a stochastic Brownian force, $\boldsymbol{F}^g_i$ is the surrounding plasma medium gravitation force and $\boldsymbol{F}^{\bar{g}}_i$ is a buoyancy force.

The principal findings which were qualitatively in good agreement with previous experimental results were that the blood clot dissolution is triggered when there is a high velocity plasma flow; the progress of blood clot dissolution is followed the removal of clot fragments that are still interconnected by a partially dissolved fibrin meshwork; and the higher plasma velocity is, the larger are the sizes of the removed fragments.

Recent studies have provided evidence of a significant role of the Hageman factor (a plasma protein which is a part of the coagulation cascade) in pathological clot formation. Since auto-activation of the Hageman factor prompts the intrinsic coagulation pathway, Shavlyugin et al. [43] studied the dynamics of pathological clot formation considering the intrinsic pathway as the predominant mechanism of this process. It was hypothesized that in many cases the rate of pathological clot formation is much lower than that of a hemostatic clot. This assumption was used to simplify the mathematical model and to estimate kinetic constants of biochemical reactions that bring about pathological clot formation. The deployed approach emphasized the effects of activated platelets on the dynamics of pathological clot formation in the following process: thrombin production, then platelet activation, then expression of phospholipids by platelets, after that, increase in the values of the kinetic constants of biochemical reactions.

In previously published models, the mechanism of platelet activation by thrombin and its effects on the functioning of the enzymatic cascade was not considered in detail, whereas the model in [43] took into account the impact of the platelet activation process on intrinsic coagulation pathway (ICP) dynamics with respect to the dependence of inferred experimental constants for enzymatic kinetics on some part of activated platelets. This model consisted of a system of ordinary differential equations, representing the mass balance of ICP reagents and equations that describe the kinetics of platelet activation by thrombin. A spatially localized process of in vivo plot coagulation formation was modeled, so that the loss of coagulation factors in plasma were not taken into consideration. Published experimental data were not available to validate the proposed mathematical model.

The contact system is the initiating subsystem of ICP whose activation in vivo is described by the following mathematical model of the contact system:

$$\frac{d[XIIa]}{dt} = k_{catXII}^{XIIa}\frac{[XIIa][XII]}{K_{mXII}^{XIIa}+[XII]} + k_{catXII}^{K}\frac{[K][XII]}{K_{mXII}^{K}+[XII]} - I_{XIIa}^{C1inh}[XIIa][C1\textit{inh}],$$
$$\frac{d[K]}{dt} = k_{catPK}^{XIIa}\frac{[XIIa][PK]}{K_{mPK}^{XIIa}+[PK]} + k_{catPK}^{PRCP}\frac{[PRCP][PK]}{K_{mPK}^{PRCP}+[PK]} - I_{K}^{C1inh}[K][C1\textit{inh}],$$

where $[XIIa]$, $[K]$ and $[PRCP]$ are the concentrations of activated Hageman factor, kallikrein and prolylcarboxypeptidase, respectively, k_{catXII}^{XIIa}, k_{catXII}^{K} and k_{catPK}^{XIIa} are the catalytic kinetic constants of the reactions implied their indices, K_{mXII}^{XIIa}, K_{mXII}^{K}, K_{mPK}^{XIIa} and K_{mPK}^{PRCP} are Michaelis constants of the reactions implied by their indices and I_{XIIa}^{C1inh} and I_{K}^{C1inh} are the kinetic constants of inhibition of Hageman factor and kallikrein, respectively. Kallirkrein and prolylcarboxypeptidase are the enzymes capable of cleaving peptide bonds in proteins; $[XII]$ and $[PK]$ are the concentrations of Hageman factor and prekallikrein (an enzyme which is cleaved to produce kallikrein by activated XII. $C1$ complement is a molecule that inhibits the activation. $[C1\textit{inh}]$ is the concentration of the inhibitor of complement $C1$)

It was claimed that known experimental studies deal only with the processes of fast clot formation (completed within a few minutes) under high thrombin concentrations. Besides, in most of the experimental studies, the effects of platelet activation are simulated by artificial injection of phospholipids which prohibited the evaluation of the effects of platelet activation kinetics whereas these effects are central in [**43**].

A more detailed study of lysis and thrombolysis process to treat the diseases resulting from occluded artheries, such as celebro-vascular stroke should be specially noticed and developing current models such as the one presented by Bajd and Serša in [**3**] could be valuable. Describing the behavior of the blood near the bifurcation of the arteries going through the brain as they become smaller and smaller would be helpful while an embolus passes through them and may result in a stroke. Moreover, seizures after stroke are more likely to happen after a severe hemorrhagic stroke or a stroke involving the part of the brain called the cerebral cortex. The most common seizures resulting from strokes occur after a delay of weeks or months. The likelihood of any stroke producing such delayed seizures is dependent on its size and location. Small strokes deeper in the brain, are unlikely to cause seizures. Larger strokes and those involving the outer surface of the brain known as the grey matter, or cortex, are more likely to cause delayed seizures. Therefore, it might be possible to prevent these types of seizures happening by appropriate treatment after larger strokes.

The stability of clots is closely related to the fibrin network, which provides the structural support for a blood clot. The viscoelastic properties of a thrombus partially occluding a vessel will determine whether the flowing blood will cause it to deform reversibly or irreversibly, rupture or

embolize. Thrombi that are very stiff or brittle might have a greater tendency to embolize, while those that are more viscose or plastic might deform to a new shape.

At low strains or deformations, stress is directly proportional to strain while at large strains, the stiffness of the clot increases up to a large factor. This phenomenon allows fibrin clots to be compliant at normal strain levels and then become stiffer at larger deformations that could otherwise threaten clot integrity. In fact, fibrin can be reversibly stretched about 4-5 times before rupture. So it means that forces imposed by the flow greater than this strength of the fibrin could cause an embolus.

Formation of an embolus generally favors arteries that receive the highest volumetric flow of blood. Previous investigations suggest that particles tend to favor wider diameter daughter branches at vessel bifurcations and this bias increases with increasing particle size. The embolic particles can be modeled as spheres and coupled to the fluid dynamics by the Maxe-Riley equation:

$$(\rho_p + \frac{1}{2}\rho_f)\left(\frac{d\mathbf{v}(x(t))}{dt}\right) = (\rho_p - \rho_f)\mathbf{g} = \frac{3}{2}\rho_f \frac{D\mathbf{u}(x(t))}{Dt} - \frac{9}{2}\frac{\mu}{a^2}\left(\mathbf{v}(x(t)) - \mathbf{u}(x(t))\right),$$

where $\mathbf{v}$ is the particle velocity, $\mathbf{u}$ is the blood velocity, $\mathbf{g}$ is gravity, a is the particle radius, μ is the blood viscosity and ρ_p and ρ_f are particle and blood densities.

The multiscale models developed so far have been mostly for 2D blood vessels. However, further study is needed to provide quantitative descriptions of thrombus development or breakdown. The ability to predict the outcomes of simultaneous variation at multiple hemostatic components will possibly enable us to more accurately evaluate hemorrhagic or thrombotic risks for patients.

As previously mentioned, Bajd and Serša [3] presented a model in which the blood clot was composed of randomly distributed, spherically shaped blood cells interconnected by elastic fibrin bonds which seems to be a practical model for clot dissolution. Each nonsuperficial cell has 6 nearest neighbor bonds, 12 next nearest neighbor bonds and 8 third next nearest neighbor bonds yielding 26 bonds/cell. All cells are randomly displaced from their original positions which is followed by calculating the equilibrium lengths of the fibrin fibers connecting neighbor blood cells. Due to the viscoelastic properties of fibrin fibers, the binding force could be modeled by a Kelvin-Voigt model as:

$$\boldsymbol{F}^b_{i,j}(t) = \left[k_{Fb}(\|\boldsymbol{r}_{i,j}(t)\| - \|\boldsymbol{r}_{i,j}(0)\|) - \eta_{Fb}\frac{\|\boldsymbol{r}_{i,j}(t) - \boldsymbol{r}_{i,j}(t-\Delta t)\|}{\Delta t}\right]\frac{\boldsymbol{r}_{i,j}(t)}{\|\boldsymbol{r}_{i,j}(t)\|},$$

where k_{Fb} and η_{Fb} correspond to effective fibrin bond stiffness (or a spring constant) and a fibrin viscous coefficient, respectively; and $\boldsymbol{r}_{i,j}(t)$ is the difference between the positions of *i*th and *j*th blood cells at time *t* ($t = 0$ indicating the initial time).

However, as the fibers in a fibrin clot are structures that have length to diameter ratio of 30-50, those predominantly deform under load by bending, rather than stretching the elements. According to

[9], assuming a homogeneous, isotropic, linearly elastic fiber, its elastic modulus by the stretching formula is given by $E = 4pL/(\pi d^2 y)$, where E is elastic modulus, p is force applied, L is effective length of fiber segment, d is the fiber diameter and y is deflection at the point load. From stretching experiments, the elastic modulus was $1.9 \pm 1.8MPa$, whereas the calculated elastic modulus for fibers was $2.6 \pm 1.5MPa$.

Particle j exerts a force on particle i if it is within a radius of influence r of particle i. Therefore, this force can be expressed as;

$$F_{ij} = a_{ij}\left(1 - \frac{r_{ij}}{r}\right)\boldsymbol{r}_{ij}^{\mathbf{0}},$$

where a_{ij} is the maximum repulsion force per unit mass, r_{ij} is the distance between i and j, $\boldsymbol{r}_{ij}^{\mathbf{0}} = \frac{\boldsymbol{r}_{ij}}{\|r_{ij}\|}$ is the unit vector pointing in direction from j to i. Two other forces also introduced as dissipative, F_{ij}^D, and random (Brownian) forces, F_{ij}^R:

$$F_{ij}^D = -\gamma w_D(\boldsymbol{v}_{ij}.\boldsymbol{e}_{ij})\boldsymbol{r}_{ij}^{\mathbf{0}},$$
$$F_{ij}^R = \sigma w_R \xi_{ij}\boldsymbol{r}_{ij}^{\mathbf{0}},$$

where γ is the friction coefficient, σ is the amplitude of the random force, w_D and w_R are the weight functions for dissipative and random forces dependent on the distance r from the particle i and ξ_{ij} is a random number with zero mean and unit variance.

The weight functions w_D and w_R can be expressed as:

$$w_D = (1 - \frac{r_{ij}}{r})^2,$$
$$w_R = (1 - \frac{r_{ij}}{r}).$$

In the work of Bajd and Serša [3], the net drag force on the spherical cell included the interaction between plasma flow and the blood clot:

$$\boldsymbol{F}_i^d(t) = -6\pi\eta_p R\left(\boldsymbol{v}_i(t) - \boldsymbol{v}_i^p\right),$$

where η_p is blood plasma viscosity, $\boldsymbol{v}_i(t)$ is the current velocity of the cell, and $\boldsymbol{v}_i^p(t)$ is the background plasma velocity at the site of the blood cell.

The net effect of the Brownian force on each cell was approximated by normally distributed vectors with variance $\sqrt{2k_BT \times 6\pi\eta_p R\delta(t-t')}$. Here, k_B is the Boltzmann constant, T is an absolute physiological temperature and $\delta(t-t')$ is the Dirac delta function.

Initial blood cell velocities were considered equal to zero and blood cells next to the vein walls remained fixed at their initial positions during all simulation steps, whereas the positions of the other cells were calculated by applying the explicit integration method at each time step. Cell

positions were calculated by the Verlet algorithm:

$$\boldsymbol{r}_i(t+\Delta t) = 2\boldsymbol{r}_i(t) - \boldsymbol{r}_i(t-\Delta t) + \frac{\Delta t^2}{m}\boldsymbol{F}_i(t),$$

and their velocities calculated by

$$\boldsymbol{v}_i(t+\Delta t) = \frac{(\boldsymbol{r}_i(t+\Delta t) - \boldsymbol{r}_i(t))}{\Delta t}.$$

The hemodynamic conditions were described by the Womersley equation, i.e., the Navier-Stokes equation for incompressible Newtonian fluid with the Stokesian approximation:

$$\rho\frac{\partial \boldsymbol{v}^p(t)}{\partial t} = -\nabla p(t) + \eta_p \Delta \boldsymbol{v}^p(t).$$

The superposition of a constant pressure gradient (with amplitude A_1) maintains a net flow rate through the vein chamber and a pulsatile sinusoidal pressure gradient which mimics heart pulsation (with amplitude A_2 and frequency $\nu = \omega/2\pi$) is given by:

$$-\nabla p(t) = A_1\mathbf{e}_y + A_2 sin(\omega t)\mathbf{e}_y.$$

The effect of bond decay between two neighboring cells referred to spatial corrosion and was also dependent on relative bond stretching (so-called deformational corrosion). A bond was removed either when it became totally degraded or when it was mechanically overstretched. Fibrin fibers are extremely elastic and they can be stretched up to 300%. Bond removal caused by overstretching was induced by the mechanical forces of streaming plasma. All the parameters of the Kelvin-Voigt model were calculated from the experimental results. We will return to the basic modeling of the thrombus using beads and springs in the next chapter.

Chapter 2

MATHEMATICAL MODELING OF THE PROBLEM

To study the behavior of the blood in an artery in the presence of an occlusion, a rectangular channel is considered in which the clot adheres to part of the lower wall (Fig. 2.1).

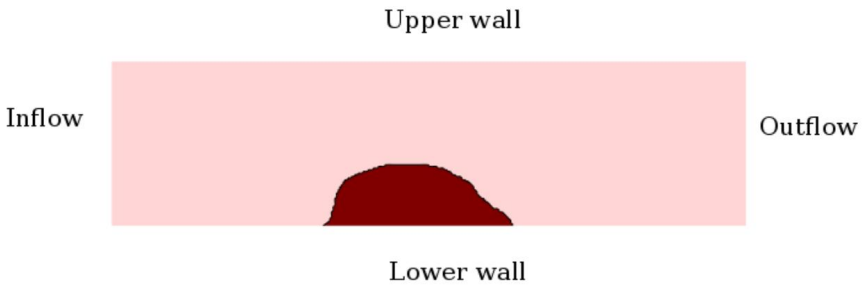

FIGURE 2.1. A rectangular channel representing an artery in the presence of a clot

2.1. FLUID MODELING: THE NAVIER-STOKES EQUATIONS

The flowing blood in our modeling will be considered as an incompressible Newtonian fluid. With this in view, we need some definitions and fundamentals to describe the behavior of the blood and now give a brief derivation of the incompressible Navier-Stokes equations, based on the treatment in Chapter 2 of Owens and Phillips [**33**].

2.1.1. Forces and equations of motion

Suppose that we have a volume $V(t)$ of infinitesimal fluid particles with a closed bounded surface $S(t)$, with an orientation $\boldsymbol{n}$, as shown in Fig. 2.2

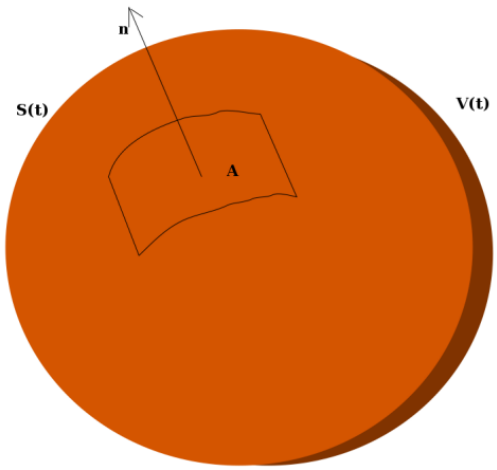

FIGURE 2.2. The material volume

We define the stress vector $\boldsymbol{s_n}(\boldsymbol{x}, t)$ as:

$$\boldsymbol{s_n}(\boldsymbol{x}, t) = \frac{\delta \boldsymbol{F}(\boldsymbol{x}, t)}{\delta S} \tag{2.1.1}$$

where $\delta \boldsymbol{F}(\boldsymbol{x}, t)$ is the force exerted at time t on the surface element A having area δS by the fluid into which $\boldsymbol{n}$ is pointing.

The total force experienced by the fluid including the force exerted on its surface and the body forces such as gravity can be written as

$$\int_{S(t)} \boldsymbol{s_n} dS + \int_{V(t)} \rho \boldsymbol{b} dV, \tag{2.1.2}$$

where ρ is the density of the fluid in $V(t)$ and $\boldsymbol{b}$ is the body force per unit mass.

Theorem 2.1.1 (The Reynolds transport theorem)**.** *Let $V(t)$ be a material volume and $G(\boldsymbol{x}, t)$ any scalar or vector function. Then*

$$\frac{d}{dt} \int_{V(t)} G dV = \int_{V(t)} \Big(\frac{DG}{Dt} + G \nabla . \boldsymbol{u} \Big) dV.$$

D/Dt is called the material derivative and defined as:

$$\frac{D}{Dt} = \frac{\partial}{\partial t} + \boldsymbol{u}(\boldsymbol{x}(t), t) . \nabla. \tag{2.1.3}$$

Applying the Reynolds transport theorem to the conservation of mass equation

$$\frac{d}{dt} \int_{V(t)} \rho dV = 0 \tag{2.1.4}$$

we obtain

$$\int_{V(t)} \Big(\frac{D\rho}{Dt} + \rho \nabla . \boldsymbol{u} \Big) dV = 0. \tag{2.1.5}$$

If we have a continuous integrand and since (2.1.5) is valid for any material volume $V(t)$, we can deduce from (2.1.5) that:

$$\frac{D\rho}{Dt} + \rho\nabla.\boldsymbol{u} = 0. \tag{2.1.6}$$

If $D\rho/Dt = 0$, we say the fluid is incompressible and from (2.1.6) we have a solenoidal velocity field, i.e.

$$\nabla.\boldsymbol{u} = 0. \tag{2.1.7}$$

Theorem 2.1.1 along with (2.1.6) are used in the principle of linear momentum (Euler),

$$\frac{d}{dt}\int_{V(t)} \rho\boldsymbol{u}dV \;=\; \int_{S(t)} \boldsymbol{s_n}dS \;+\; \int_{V(t)} \rho\boldsymbol{b}dV, \tag{2.1.8}$$

$$\Rightarrow \qquad \int_{V(t)} \left(\frac{D(\rho\boldsymbol{u})}{Dt} + \rho\boldsymbol{u}\nabla.\boldsymbol{u}\right) dV = \int_{S(t)} \boldsymbol{s_n}dS \;+\; \int_{V(t)} \rho\boldsymbol{b}dV, \tag{2.1.9}$$

$$\Rightarrow \qquad \int_{V(t)} \left(\rho\frac{D\boldsymbol{u}}{Dt} + \boldsymbol{u}\frac{D\rho}{Dt} + \rho\boldsymbol{u}\nabla.\boldsymbol{u}\right) dV = \int_{S(t)} \boldsymbol{s_n}dS \;+\; \int_{V(t)} \rho\boldsymbol{b}dV, \tag{2.1.10}$$

$$\Rightarrow \qquad \int_{V(t)} \left(\rho\frac{D\boldsymbol{u}}{Dt}\right) + \boldsymbol{u}\left(\frac{D\rho}{Dt} + \rho\nabla.\boldsymbol{u}\right) dV = \int_{S(t)} \boldsymbol{s_n}dS \;+\; \int_{V(t)} \rho\boldsymbol{b}dV, \tag{2.1.11}$$

$$\Rightarrow \qquad \int_{V(t)} \rho\frac{D\boldsymbol{u}}{Dt}\, dV = \int_{S(t)} \boldsymbol{s_n}dS \;+\; \int_{V(t)} \rho\boldsymbol{b}dV. \tag{2.1.12}$$

2.1.1.1. *The stress tensor*

From equation (2.1.12) the existence of a stress tensor $\boldsymbol{\sigma}$ having the following property can be proved:

$$\boldsymbol{s_n}(\boldsymbol{x}, t) \;=\; \boldsymbol{n}.\boldsymbol{\sigma}. \tag{2.1.13}$$

Theorem 2.1.2. *Let $\mathscr{D}$ be a bounded region in $\mathbb{R}^3$ and let $\boldsymbol{s_n}(\boldsymbol{x}, t)$ be a stress vector defined throughout $\mathscr{D}$. There exists a second-order stress tensor $\boldsymbol{\sigma}(\boldsymbol{x}, t)$ such that throughout $\mathscr{D}$,*

$$\boldsymbol{s}_n \;=\; \boldsymbol{n}.\boldsymbol{\sigma}, \tag{2.1.14}$$

$$\boldsymbol{\rho}\frac{D\boldsymbol{u}}{Dt} \;=\; \nabla.\boldsymbol{\sigma} + \rho\boldsymbol{b}, \tag{2.1.15}$$

$$\boldsymbol{\sigma} \text{ is symmetric.} \tag{2.1.16}$$

PROOF. See [33]. □

In fact, substituting (2.1.14) into Eqn. (2.1.12) and using the divergence theorem on the right-hand side of (2.1.12), we can obtain (2.1.15).

2.1.2. The Newtonian fluid

A Newtonian fluid is one for which there is a simple linear relationship between the stress and the rate of strain. The stress tensor $\boldsymbol{\sigma}$ in (2.1.15) has a particular form and we proceed to explain how to derive it. The components σ_{ij} of $\boldsymbol{\sigma}$ are of the form:

$$\sigma_{ij} = -p\delta_{ij} + T_{ij}, \tag{2.1.17}$$

where δ_{ij} the Kronecker δ, the pressure p and the linear function $\boldsymbol{T}$ so-called deviatoric stress or extra-stress are in the form:

$$\delta_{ij} = \begin{cases} 0, & \text{if } i \neq j, \\ 1, & \text{if } i = j \end{cases} \tag{2.1.18}$$

$$p = -\frac{1}{3}\sum_{i=1}^{3}\sigma_{ii} \tag{2.1.19}$$

$$T_{ij} = A_{ijkl}\frac{\partial u_k}{\partial x_l}, \qquad \text{(the components of } \boldsymbol{T}) \tag{2.1.20}$$

where $\boldsymbol{A}$ is an isotropic fourth-order tensor, i.e. its physical properties are independent of direction.

Since $\boldsymbol{A}$ is isotropic we may write the components A_{ijkl} of $\boldsymbol{A}$ in the form:

$$A_{ijkl} = \lambda\delta_{ij}\delta_{kl} + \mu\delta_{ik}\delta_{jl} + \nu\delta_{il}\delta_{jk}, \tag{2.1.21}$$

where λ, μ and ν are constants. From Theorem 2.1.2 we see that $\boldsymbol{T}$ in (2.1.17) is symmetric and therefore, from (2.1.20) $\boldsymbol{A}$ must be symmetric in its first two indices. Then, we can reduce (2.1.21) to:

$$A_{ijkl} = \lambda\delta_{ij}\delta_{kl} + \mu(\delta_{ik}\delta_{jl} + \delta_{il}\delta_{jk}) \qquad (\mu = \nu), \tag{2.1.22}$$

and from (2.1.20):

$$\begin{aligned} T_{ij} &= \lambda\delta_{ij}\frac{\partial u_k}{\partial x_k} + \mu\Big(\frac{\partial u_i}{\partial x_j} + \frac{\partial u_j}{\partial x_i}\Big), \\ &= \frac{\lambda}{2}\delta_{ij}\sum_{k=1}^{3}\dot{\gamma}_{kk} + \mu\dot{\gamma}_{ij}, \end{aligned} \tag{2.1.23}$$

where $\dot{\gamma}_{ij}$ is the ijth component of the rate of strain tensor $\dot{\boldsymbol{\gamma}}$ given by:

$$\dot{\boldsymbol{\gamma}} = \Big(\nabla\boldsymbol{u} + (\nabla\boldsymbol{u})^T\Big). \tag{2.1.24}$$

Taking $i = j$ in (2.1.17) and the definition of p in (2.1.19) we have:

$$\sum_{i=1}^{3} \sigma_{ii} = -3p + \sum_{i=1}^{3} T_{ii} \qquad \Rightarrow \qquad \sum_{i=1}^{3} T_{ii} = 0, \tag{2.1.25}$$

Therefore, from (2.1.23)

$$\sum_{i=1}^{3} T_{ii} = \frac{3}{2}\lambda \sum_{i=1}^{3} \dot{\gamma}_{ii} + \mu \sum_{i=1}^{3} \dot{\gamma}_{ii} = 0 \tag{2.1.26}$$

$$\Rightarrow \qquad 3\lambda + 2\mu = 0, \tag{2.1.27}$$

so that,

$$T_{ij} = -\frac{1}{3}\mu\dot{\gamma}_{kk}\delta_{ij} + \mu\dot{\gamma}_{ij}. \tag{2.1.28}$$

Since

$$\sum_{k=1}^{3} \dot{\gamma}_{kk} = 2\sum_{k=1}^{3} \frac{\partial u_k}{\partial x_k} = 2\nabla.\boldsymbol{u} = 0, \tag{2.1.29}$$

therefore, for an incompressible fluid (2.1.17) becomes:

$$\sigma_{ij} = -p\delta_{ij} + \mu\dot{\gamma}_{ij}. \tag{2.1.30}$$

Finally, by inserting (2.1.30) into (2.1.15) we obtain the equation of motion for a Newtonian fluid:

$$\rho\frac{Du_i}{Dt} = -\frac{\partial p}{\partial x_i} + \mu\frac{\partial}{\partial x_j}\Big(\frac{\partial u_i}{\partial x_j} + \frac{\partial u_j}{\partial x_i}\Big) + \rho b_i, \tag{2.1.31}$$

$$= -\frac{\partial p}{\partial x_i} + \mu\frac{\partial^2 u_i}{\partial x_j^2} + \rho b_i. \tag{2.1.32}$$

Hence, the vector form of the Navier-Stokes equations for an incompressible fluid is given by:

$$\rho\frac{D\boldsymbol{u}}{Dt} = -\nabla p + \mu\nabla^2\boldsymbol{u} + \rho\boldsymbol{b}. \tag{2.1.33}$$

2.1.3. The two-dimensional Navier-Stokes equations

As mentioned previously, we suppose that the blood is a Newtonian fluid. From (2.1.33) the incompressible Navier-Stokes equations in two dimensions in a rectangular domain for a Newtonian fluid can be written as:

$$\rho\left(\frac{\partial u}{\partial t} + u\frac{\partial u}{\partial x} + v\frac{\partial u}{\partial y}\right) = -\frac{\partial p}{\partial x} + \mu\left(\frac{\partial^2 u}{\partial x^2} + \frac{\partial^2 u}{\partial y^2}\right) + F_x \tag{2.1.34}$$

$$\rho\left(\frac{\partial v}{\partial t} + u\frac{\partial v}{\partial x} + v\frac{\partial v}{\partial y}\right) = -\frac{\partial p}{\partial y} + \mu\left(\frac{\partial^2 v}{\partial x^2} + \frac{\partial^2 v}{\partial y^2}\right) + F_y \tag{2.1.35}$$

$$u_x + v_y = 0 \tag{2.1.36}$$

where u and v are horizontal and vertical components of fluid velocity, respectively; p is the fluid pressure; ρ is the fluid density; μ is the dynamic viscosity and $\boldsymbol{F} = (F_x, F_y)$ is the force exerted by the clot boundary on the fluid. We denote the fluid velocity by $\boldsymbol{u} := (u, v)$ and introduce a characteristic velocity U, characteristic time T and characteristic length L (the way these are calculated will be described in the next section) and non-dimensionalize the Navier-Stokes equations as follows:

$$\boldsymbol{u}^* = \frac{\boldsymbol{u}}{U}, \quad t^* = \frac{t}{T}, \quad x^* = \frac{x}{L} \text{ and } y^* = \frac{y}{L} \tag{2.1.37}$$

where an asterisk on a variable indicates that it is dimensionless. From (2.1.34)

$$\frac{U\rho}{T}\frac{\partial u^*}{\partial t^*} + \frac{\rho U^2}{L}u^*\frac{\partial u^*}{\partial x^*} + \frac{\rho U^2}{L}v^*\frac{\partial u^*}{\partial y^*} = - \frac{1}{L}\frac{\partial p}{\partial x^*} + \frac{\mu U}{L^2}\left(\frac{\partial^2 u^*}{\partial x^{*2}} + \frac{\partial^2 u*}{\partial y^{*2}}\right) + F_x \tag{2.1.38}$$

$$\Rightarrow \quad \frac{\partial u^*}{\partial t^*} + u^*\frac{\partial u^*}{\partial x^*} + v^*\frac{\partial u^*}{\partial y^*} = -\frac{1}{\rho U^2}\frac{\partial p}{\partial x^*} + \frac{\mu}{L\rho U}\left(\frac{\partial^2 u^*}{\partial x^{*2}} + \frac{\partial^2 u*}{\partial y^{*2}}\right) + \frac{T}{\rho U}F_x \tag{2.1.39}$$

Here we are assuming that $T = L/U$. We now define $p^* := p/\rho u^2$ and $Re = L\rho U/\mu$ and $F_x^* = (T/\rho U)F_x$, so that (2.1.39) becomes

$$\frac{\partial u^*}{\partial t^*} + u^*\frac{\partial u^*}{\partial x^*} + v^*\frac{\partial u^*}{\partial y^*} = -\frac{\partial p^*}{\partial x^*} + \frac{1}{Re}(\frac{\partial^2 u^*}{\partial x^{*2}} + \frac{\partial^2 u*}{\partial y^{*2}}) + F_x^* \tag{2.1.40}$$

Similarly, from (2.1.35) we have

$$\frac{\partial v^*}{\partial t^*} + u^*\frac{\partial v^*}{\partial x^*} + v^*\frac{\partial v^*}{\partial y^*} = -\frac{\partial p^*}{\partial y^*} + \frac{1}{Re}(\frac{\partial^2 v^*}{\partial x^{*2}} + \frac{\partial^2 v*}{\partial y^{*2}}) + F_y^* \tag{2.1.41}$$

Finally, (2.1.36) becomes

$$\frac{\partial u^*}{\partial x^*} + \frac{\partial v^*}{\partial y^*} = 0 \tag{2.1.42}$$

Eqn. (2.1.36) allows us to write down an alternative form of Eqns. (2.1.40)-(2.1.41):

$$u^*\frac{\partial u^*}{\partial x^*} + v^*\frac{\partial u^*}{\partial y^*} = \frac{\partial u^{*2}}{\partial x^*} + \frac{\partial (u^*v^*)}{\partial y^*} \tag{2.1.43}$$

$$u^*\frac{\partial v^*}{\partial x^*} + v^*\frac{\partial v^*}{\partial y^*} = \frac{\partial (u^*v^*)}{\partial x^*} + \frac{\partial v^{*2}}{\partial y^*} \tag{2.1.44}$$

Therefore, the non-dimensionalized Navier-Stokes equations with some rearrangements can be rewritten as follows

$$\frac{\partial u^*}{\partial t^*} + \frac{\partial p^*}{\partial x^*} = -\left(\frac{\partial u^{*2}}{\partial x^*} + \frac{\partial (u^* v^*)}{\partial y^*}\right) + \frac{1}{Re}\left(\frac{\partial^2 u^*}{\partial x^{*2}} + \frac{\partial^2 u*}{\partial y^{*2}}\right) + F_x^* \tag{2.1.45}$$

$$\frac{\partial v^*}{\partial t^*} + \frac{\partial p^*}{\partial y^*} = -(\frac{\partial (u^* v^*)}{\partial x^*} + \frac{\partial v^{*2}}{\partial y^*}) + \frac{1}{Re}\left(\frac{\partial^2 v^*}{\partial x^{*2}} + \frac{\partial^2 v*}{\partial y^{*2}}\right) + F_y^* \tag{2.1.46}$$

$$\frac{\partial u^*}{\partial x^*} + \frac{\partial v^*}{\partial y^*} = 0 \tag{2.1.47}$$

To solve this system of equations, we have the following boundary conditions (Fig. (2.3))

1. On inflow we impose Dirichlet conditions on the velocity components u and v obtained from the exact solutions to start up Poiseuille flow in a channel, with initial velocity zero and a constant pressure gradient $\partial p/\partial x = \tilde{K}$ (for a certain $\tilde{K}$).

2. On outflow a homogeneous Dirichlet condition on the component v, a Neumann condition on the pressure $\partial p/\partial x = \tilde{K}$ and a homogeneous Neumann condition on the component u are imposed;

3. On the upper and the lower walls we have no-slip and no-penetration boundary conditions and a homogeneous Neumann condition on the pressure.

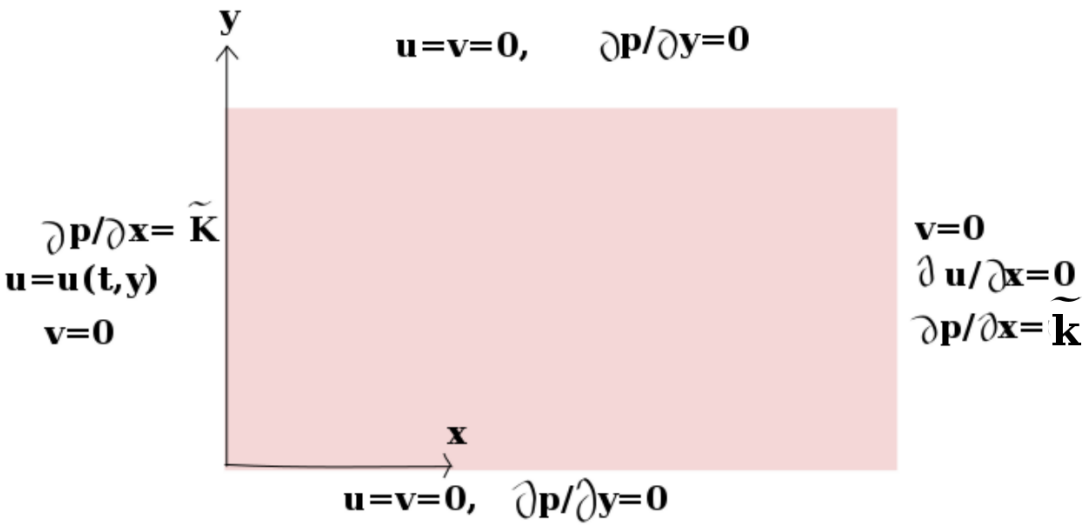

FIGURE 2.3. The boundary conditions on the flow.

The pressure is defined as

$$p = Kx + p_0 + \tilde{p} \tag{2.1.48}$$

where K is an imposed pressure gradient and $\tilde{p}$ is the excess pressure which should tend to zero as $t \to \infty$.

The Dirichlet boundary condition for the flow velocity's horizontal component on inflow is the solution of the following nonhomogeneous equation

$$\frac{\partial u}{\partial t} = -\tilde{K} + \frac{1}{Re}\frac{\partial^2 u}{\partial y^2}$$

where u is the horizontal component of the flow velocity and $\tilde{K} := \frac{K}{Re}$ is the dimensionless pressure gradient on inflow (we assume that $\frac{\partial \tilde{p}}{\partial x} = 0$).

To solve this equation, we treat a particular solution $u_p = u_p(y)$ such that

$$\frac{\partial^2 u_p}{\partial y^2} = K$$

and by integrating both sides we have

$$\frac{\partial u_p}{\partial y} = Ky + c_1, \qquad \text{for some constant } c_1.$$

Now, we would like to have $\frac{\partial u_p}{\partial y} = 0$ when $y = 1/2$, so that

$$\frac{\partial u_p}{\partial y} = K\left(y - \frac{1}{2}\right).$$

Integrating again

$$u_p = K\left(\frac{y^2}{2} - \frac{1}{2}y\right) + c_2 \qquad \text{for some constant } c_2,$$

with the boundary condition $u_p(0) = 0$, we therefore get

$$u_p = \frac{K}{2}y(y-1),$$

and we see that $u_p(1) = 0$ as well as $u_p(0) = 1$ because we have no-slip boundary conditions on the upper and lower walls.

Now solve $\frac{\partial u_h}{\partial t} = \frac{1}{Re}\frac{\partial^2 u_h}{\partial y^2}$, where the homogeneous solution $u_h = u(t, y)$. And solve the equation via the method of separation of variables, i.e., we write $u_h = f(t)g(y)$ for functions f and g to be determined.

$$f'g = \frac{1}{Re}fg''$$

$$\Rightarrow \qquad Re\frac{f'}{f} = \frac{g''}{g} = \lambda$$
$$\Rightarrow \qquad f(t) = Ae^{\frac{\lambda}{Re}t} \qquad \text{(and to have a decreasing solution we choose } \lambda = -k^2\text{)}$$

and

$$\frac{g''}{g} = -k^2$$
$$\Rightarrow \qquad g(y) = A\cos(ky) + B\sin(ky).$$

$u_h(t, y = 0 \; or \; y = 1) = 0$, therefore, $A = 0$ when $y = 0$ and $B\sin(ky) = 0$ when $y = 1$. By choosing $k = n\pi$ such that $n \in \mathbb{N}$, the solution is

$$u_h(t, y) = \sum_{n=1}^{\infty} B_n \sin(n\pi y) e^{-\frac{n^2\pi^2}{Re}t},$$

And the complete solution is

$$u(t, y) = \frac{Ky}{2}(y - 1) + \sum_{n=1}^{\infty} B_n \sin(n\pi y) e^{(-\frac{n^2\pi^2}{Re}t)}.$$

We require $u(t = 0, y) = 0$,

$$\Rightarrow \frac{Ky}{2}(y - 1) + \sum_{n=1}^{\infty} B_n \sin(n\pi y) = 0,$$

Multiplying both sides by $\sin(m\pi y)$ and integrating from 0 to 1 we have

$$\frac{K}{2}\int_0^1 y(y - 1)\sin(m\pi y\, dy) + \frac{B_m}{2} = 0.$$

Having simplified the equality, it gives $B_m = \frac{4K}{m^3\pi^3}$ for odd values of m. Hence, the dimensionless time-dependent function u is

$$u(t, y) = \frac{K}{2}y(y - 1) + \frac{4K}{\pi^3}\sum_{n\,odd}\frac{1}{n^3}\sin(n\pi y)e^{-\frac{n^2\pi^2}{Re}t}.$$

In order that the average value of the streamwise velocity be 1 in fully developed flow we require

$$\frac{K}{2}\int_0^1 (y^2 - y)\, dy = 1$$
$$\Rightarrow \qquad -\frac{K}{12} = 1$$
$$\Rightarrow \qquad K = -12.$$

Thus, $\tilde{K} = K/Re = -12/Re$.

2.2. MODELING OF THE SOLID

A clot may be viewed as an ensemble of particles that are interconnected by fibrin fibers. The fibrin fibers of a clot are viscoelastic materials. That is, they have both viscous properties of viscous fluids and elastic properties of elastic solids. Therefore, we consider the clot as a system of beads and springs in which the former represents the clot particles (red cells) and the latter represents the fibrin fibers (Fig 2.4). Elastic materials behave like a spring. That is, they deform and recover from

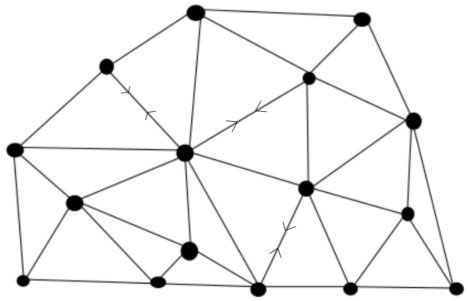

FIGURE 2.4. A bead-spring schematic representation of a clot

deformation in a similar way. For a Hookean elastic material, the stress is proportional to the strain (see Fig. 2.5) [30].

$$\sigma = E\varepsilon \tag{2.2.1}$$

where σ is the applied force divided by the cross-sectional area of the material, E is the elastic modulus and ε is the strain variable.

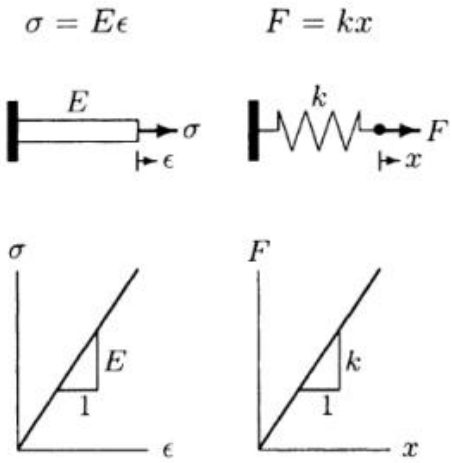

FIGURE 2.5. A comparison between an elastic material and a linear spring

For a Newtonian fluid, stresses are dependent upon the strain rates. Water and blood plasma are examples of such fluids. For these fluids,

$$\sigma = \eta\dot{\varepsilon} \qquad \left(\dot{\varepsilon} = \frac{d\varepsilon}{dt}\right)$$

where η is the coefficient of viscosity which is the constant of proportionality between the stress σ and the strain rate $\dot{\varepsilon}$. Fig. 2.6 shows the $\sigma - \dot{\varepsilon}$ graph of a Newtonian fluid [30].

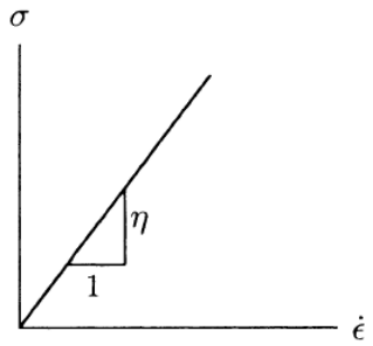

FIGURE 2.6. Stress-strain rate graph for a Newtonian fluid

There are two basic mechanical elements used to simulate the mechanical behavior of a material: the spring and the dashpot. A dashpot is a simple piston-cylinder. For a dashpot, the applied force F is linearly dependent on the rate of displacement $\dot{x}$ (see Fig. 2.7) [30],

$$F = \mu\dot{x} \qquad (\dot{x} = \frac{dx}{dt}) \tag{2.2.2}$$

where μ is the coefficient of friction.

2.2.1. Viscoelastic models

In a linear spring and a linear dashpot, a constant applied force produces a constant deformation and a constant rate of deformation, respectively. However, a spring deformation is completely recoverable, whereas in a dashpot the deformation is permanent. Various combinations of springs and dashpots are used to construct viscoelastic models. Here we discuss two of these models.

2.2.1.1. *The Kelvin-Voigt model*

A parallel system of a spring and a dashpot is called the Kelvin-Voigt model in which the total stress produced by the system

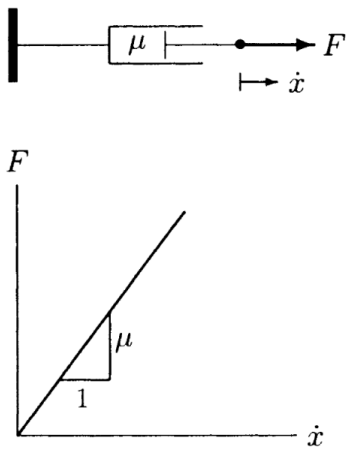

FIGURE 2.7. A linear dashpot

$$\sigma = \sigma_{spring} + \sigma_{dashpot} \tag{2.2.3}$$

will deform the spring and the dashpot equally because of their parallel setting. Therefore, the strain ϵ of the system is equal to the strain of the spring and the strain of the dashpot (Fig. 2.8) [30],

$$\varepsilon = \epsilon_{spring} = \epsilon_{dashpot} \tag{2.2.4}$$

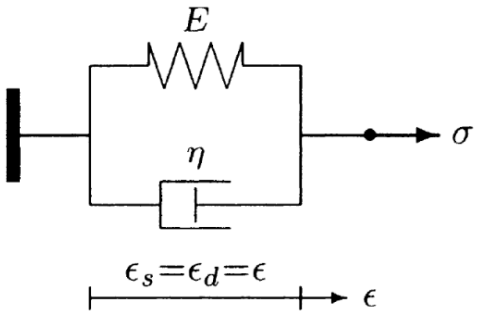

FIGURE 2.8. Kelvin-Voigt model; $\epsilon_s := \epsilon_{spring}$; $\epsilon_d := \epsilon_{dashpot}$; $\epsilon := \epsilon$

From now on, $\sigma_s := \sigma_{spring}$ and $\sigma_d := \sigma_{dashpot}$ stand for the spring and the dashpot stresses, respectively. The combination of (2.2.3) and (2.2.4) results in:

$$\sigma_s = E\varepsilon_s \tag{2.2.5}$$

$$\sigma_d = \eta\dot{\varepsilon}_d \tag{2.2.6}$$

$$\Rightarrow \quad \sigma = E\varepsilon_s + \eta\dot{\varepsilon}_d \tag{2.2.7}$$

$$\Rightarrow \quad \sigma = E\varepsilon + \eta\dot{\varepsilon} \tag{2.2.8}$$

2.2.1.2. *The Maxwell model*

The Maxwell model is a configuration of a spring and a dashpot in series (Fig. 2.9) [**30**]. In this model, the stress applied to the whole system is the same as the stresses applied to the spring and to the dashpot and the strain is the sum of the strains in the spring and the dashpot,

$$\sigma = \sigma_s = \sigma_d \tag{2.2.9}$$

$$\epsilon = \epsilon_s + \epsilon_d \tag{2.2.10}$$

$$\Rightarrow \quad E\eta\dot{\epsilon} = \eta(E(\dot{\epsilon_s}) + E(\eta\dot{\epsilon_d}) \tag{2.2.11}$$

$$\Rightarrow \quad E\eta\dot{\epsilon} = \eta\dot{\sigma} + E\sigma \tag{2.2.12}$$

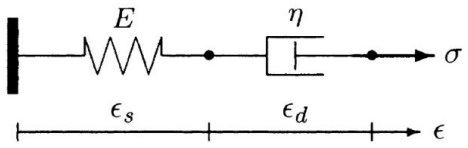

FIGURE 2.9. Maxwell model; $\epsilon_s := \epsilon_{spring}$; $\epsilon_d := \epsilon_{dashpot}$; $\epsilon := \epsilon$

2.2.2. Clot model

When we represent the elastic solid materials with springs and apply a constant stress, there is a limit to how much the Hookean spring will deform. On the other hand, a dashpot representing a viscous fluid deforms continuously as long as there is a force. Therefore, in a Maxwell model, a force applied on the system deforms both the spring and the dashpot. The spring deformation is limited, but the dashpot keeps deforming while the force is exerted. Therefore, a Maxwell model is more like a viscoelastic fluid than a solid. We saw in the Kelvin-Voigt model there is an equal strain in the dashpot and the spring. Therefore, it causes a limited deformation of the dashpot because the spring can undergo a restricted deformation. Consequently, the Kelvin-Voigt model is more like a viscoelastic solid.

The fibrin fibers of a clot are viscoelastic materials. That is, they have both viscous properties of viscous fluids and elastic solids. Therefore, from what has been discussed above, the Kelvin-Voigt model may describe the stress applied on the clot particles very well. The only force exerted by

the clot boundary on the fluid is due to the binding force arising from stretch and motion of fibrin fibers interconnecting neighboring blood cells in the clot. This model is a modified version of the Kelvin-Voigt model by Bajd and Serša [3]:

$$\boldsymbol{F}_{i,j} = \Big[\kappa(\|\boldsymbol{r}_{i,j}(t)\| - \|\boldsymbol{r}_{i,j}(0)\|) + \eta\frac{\|\boldsymbol{r}_{i,j}(t)\| - \|\boldsymbol{r}_{i,j}(t-\Delta t)\|}{\Delta t}\Big]\frac{\boldsymbol{r}_{i,j}(t)}{\|\boldsymbol{r}_{i,j}(t)\|} \tag{2.2.13}$$

where κ and η are the effective fibrin-bond stiffness (or a spring constant) and the fibrin viscous coefficient, respectively. $\boldsymbol{r}_{i,j}(t) = \boldsymbol{r}_j(t) - \boldsymbol{r}_i(t)$ and $\boldsymbol{r}_{ij}(0) = \boldsymbol{r}_j(0) - \boldsymbol{r}_i(0)$ represent the current and initial distance respectively between two neighboring blood cells i and j. For the sake of simplicity, each blood cell in the clot is considered a massless particle. The modified Kelvin-Voigt model is resistant only against the stretch [29]. Fibrin fibers are extremely elastic and can be stretched up to several times their initial distance at rest. Following Bajd and Serša [3] we apply the following criterion to snap a bond:

$$\left\|\frac{\boldsymbol{r}_{ij}(t)}{\boldsymbol{r}_{ij}(0)}\right\| \geqslant 3.$$

The clot boundary moves under the influence of the background fluid. Therefore, the interior particles will also move until they reach an equilibrium state. Consequently, in order that any interior particle finds its new equilibrium position the net force exerted by all the connected neighboring particles j should be zero (Fig. 2.10). In another words, we solve the following equation to find a new position for particle i in equilibrium with the others:

$$\sum_j \Big[\kappa\Big(\|\tilde{\boldsymbol{r}}_{i,j}(t)\| - \|\boldsymbol{r}_{i,j}(0)\|\Big) + \eta\frac{\|\tilde{\boldsymbol{r}}_{i,j}(t) - \boldsymbol{r}_{i,j}(t-\Delta t)\|}{\Delta t}\Big]\frac{\tilde{\boldsymbol{r}}_{i,j}(t)}{\|\tilde{\boldsymbol{r}}_{i,j}(t)\|} = \boldsymbol{0} \tag{2.2.14}$$

where $\tilde{\boldsymbol{r}}_{i,j} = (x_i^{new}, y_i^{new}) - (x_j, y_j)$ and j runs over all the neighboring particles connected to particle i. The precise way that we solve (2.2.14) numerically will be described in Section 3.3. Let $\boldsymbol{X}_i$ be the position of any particle i on the clot boundary. The net force $\boldsymbol{F}_i$ felt by this particle is the sum of the binding forces (2.2.13) between this particle and all the connected neighboring particles j.

Let $\boldsymbol{f}(s,t)$ be a Lagrangian force density with respect to the arc length s of the boundary of the clot at time t. We denote $\boldsymbol{X}(s,t)$ the position vector at time t of a material point on the surface having label s (see Fig. 2.11). Then, the Eulerian force density exerted at a point having position vector $\boldsymbol{x}$ is

$$\boldsymbol{F}(\boldsymbol{x},t) = \int_0^L \boldsymbol{f}(s,t)\delta(\boldsymbol{x} - \boldsymbol{X}(s,t))ds \tag{2.2.15}$$

where L is the arc length of the clot boundary. We evaluate $\boldsymbol{f}$ at each boundary particle $\boldsymbol{X}_i$ and we denote this by $\boldsymbol{f}_i$. Then, we approximate the Eulerian force density as follows.

$$\boldsymbol{F}(\boldsymbol{x},t) \approx \sum_i \boldsymbol{f}_i\delta_h\Big(\boldsymbol{x} - \boldsymbol{X}_i\Big)\Delta s_i \tag{2.2.16}$$

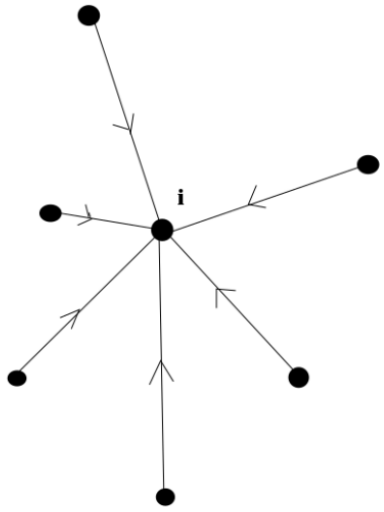

FIGURE 2.10. The forces exerted on an interior particle by the connected neighboring particles.

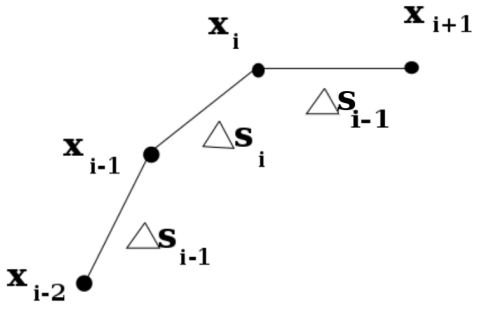

FIGURE 2.11. The clot boundary

$$\approx \sum_i \boldsymbol{F}_i \delta_h\Big(\boldsymbol{x} - \boldsymbol{X}_i\Big) \tag{2.2.17}$$

where $\boldsymbol{F}_i = \sum_j \boldsymbol{F}_{ij}$, $\boldsymbol{F}_{ij}$ being as in (2.2.13) and j running over all particles connected to the ith particle. δ_h denotes a regularized approximation to the two-dimensional delta function (see Chapter 3 , Section 3.2).

Remember that $\boldsymbol{F}^* = \frac{T}{\rho U}\boldsymbol{F}$ (see (2.1.40)-(2.1.41)). Therefore, we can non-dimensionalize the net force density $\boldsymbol{F}_i$:

$$\frac{T}{\rho U}\boldsymbol{F}_i \frac{\delta_h^*}{L^2} = \frac{T}{\rho U}\sum_j \boldsymbol{F}_{i,j}\frac{\delta_h^*}{L^2} \tag{2.2.18}$$

$$= \Big[\kappa \frac{L^2}{\rho U^2}\frac{1}{L^2}\Big(\|\boldsymbol{r}^*_{i,j}(t)\| - \|\boldsymbol{r}^*_{i,j}(0)\|\Big) \tag{2.2.19}$$

$$+ \eta \frac{L}{\rho U}\frac{1}{L^2}\frac{\|\boldsymbol{r}^*_{i,j}(t) - \boldsymbol{r}^*_{i,j}(t-\Delta t)\|}{\Delta t*}\Big]\frac{\boldsymbol{r}^*_{i,j}(t)}{|\boldsymbol{r}^*_{i,j}(t)|}\delta^*_h \tag{2.2.20}$$

where L, U and T are the characteristic length, velocity and time, respectively, and $\delta^*_h = L^2\delta_h$.

Table 2.I helps us to calculate the characteristic velocity U, and consequently, having in hand the Reynolds number value and the known values of the fluid density and viscosity, a characteristic length L is obtained.

Therefore, the non-dimensionalized effective fibrin-bond stiffness κ^* and fibrin viscous coefficient $\eta*$ are defined as follows:

$$\kappa^* = \kappa\frac{1}{\rho U^2} \qquad \& \qquad \eta^* = \eta\frac{1}{\rho U L}. \tag{2.2.21}$$

The extent to which the fluid penetrates the boundary of the clot depends on the density of the boundary particles. Ideally, we would prefer no fluid to penetrate the clot. Otherwise, Darcy's law should be taken into account which calculates the permeability of a porous medium. The fibrin spring constant, $\kappa = 0.013N/m$, and viscous coefficient of a fibrin, $\eta = 1.4 \times 10^{-3}N/(m/s)$, in the Kelvin-Voigt model are taken from [3]. The Navier-Stokes equations are solved with respect to five sets of entries for the channel diameter, mean flow, blood density and Reynolds number for a common carotid artery shown in Table 2.I.

TABLE 2.I. Common carotid artery parameters for the study models; Modified idealized: idealized normal carotid bifurcation model; Modified in vivo I & II: the right carotid bifurcations of the 28 and 32 year old volunteers, respectively [27]; Test I is for comparing the results with idealized case.

Model	Diameter (mm)	Mean flow (ml/s)	Reynolds number	Density ($\mathrm{kg/m^3}$)	Viscosity (Pa.s)
Modified idealized	6.3	6.0	346	1035	1.4×10^{-3}
Modified in vivo I	6.3	6.0	444	1035	1.4×10^{-3}
Modified in vivo II	6.3	6.0	360	1035	1.4×10^{-3}
Test I	6.3	6.0	100	1035	1.4×10^{-3}

The clot's deformation and break down are studied for each set of parameters. The spring constant and the viscous coefficient are considered with the multiplicative factors 10^4 and 10^5 for comparing the results for a clot with a less rigid structure and for a more rigid one. All the equations are dimensionless, the ratio of the dimensions of the channel (width to length) is 1:5 and as explained in Section 2.1.3, the imposed pressure gradient is calculated so that the average of horizontal velocity component is equal to 1.

Chapter 3

NUMERICAL APPROACH

In this chapter, in order to solve the Navier-Stokes equations for the blood passing through a channel in the presence of a clot, two numerical methods are used. The first one is a projection scheme to discretize the Navier-Stokes equations [40] and the second one is the immersed boundary method [36]. Therefore, the algorithm utilized here is a combination of these two methods to calculate the force $\boldsymbol{F}$ exerted by the clot boundary on the surrounding fluid by applying the immersed boundary method and consequently, by substituting the resulting force in the Navier-Stokes equations, we are able to find the velocity everywhere in the channel. The fibrin fibers are the bonds between the clot's particles. When the clot's boundary moves under the influence of the background blood, the boundary experiences some deformation which leads to the movement of all the interior particles as well. In other words, when any points on the boundary move, the net binding force exerted by the connected neighboring particles on each interior particle is not zero any more. So, they move until they reach an equilibrium state, that is, until the net binding force is zero. The rectangular channel is meshed into small rectangles of the same size. Moreover, the clot is considered as an ensemble of massless points whose positions are not compatible with the channel's meshgrid. The structure of the clot is defined by the fibrin bonds between the particles. If any bond on the boundary snaps, the boundary should be reconfigured. This means that some of the fibrin fibers and the particles attached to them which were previously inside the boundary may now appear on the reconfigured boundary. We define all the initial connections, i.e., the fibrin fibers between the clot particles, using Delaunay triangulation. Therefore, the particles are the vertices of the triangles such that no particle lies on any triangle's side or inside the circumcircle of any triangle (Fig. 3.1).

3.1. PROJECTION SCHEMES

The theoretical background of projection method for solving the incompressible Navier-Stokes equations is the Helmholtz-Hodge decomposition theorem.

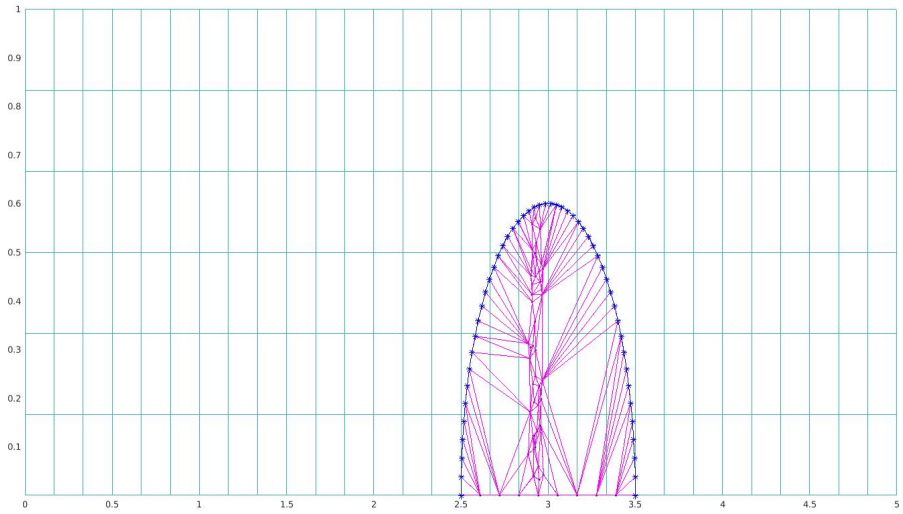

FIGURE 3.1. A clot inside a channel at $t = 0$

Theorem 3.1.1. *If $\boldsymbol{u}$ is a vector field in a simply connected domain, it can be decomposed into a divergence-free (solenoidal) part $\boldsymbol{u}_{sol}$ and an irrotational part $\boldsymbol{u}_{irrot}$.*
Thus,

$$\boldsymbol{u} = \boldsymbol{u}_{sol} + \boldsymbol{u}_{irrot} = \boldsymbol{u}_{sol} + \nabla\phi \tag{3.1.1}$$

where $\nabla\phi := \boldsymbol{u}_{irrot}$ for some scalar function ϕ. Since $\nabla \times \nabla\phi = 0$, taking the divergence of Eqn. (3.1.1) gives:

$$\nabla.\boldsymbol{u} = \nabla^2\phi \qquad \textit{(since, } \nabla.\boldsymbol{u}_{sol} = 0\textit{).}$$

The fractional-step projection method was first introduced by Chorin [7, 8] for solving the Navier-Stokes equations. The main idea of the projection method is described in two steps:

1. An intermediate velocity $\tilde{\boldsymbol{u}}$ is calculated without considering the pressure term and incompressibility.

2. A Poisson equation for the pressure is solved. This step is equivalent to a projection of $\tilde{\boldsymbol{u}}$ onto the space of incompressible velocity fields.

Chorin proposed a simple pressure-correction scheme. In this method the implicit Euler time stepping is used. The algorithm is as follows [20]:

1. Set the initial condition $\boldsymbol{u}^0 = \boldsymbol{u}_0$.

2. Let a superscript denote the time step counter and solve the following equations to compute $\tilde{\boldsymbol{u}}$, $\boldsymbol{u}^{k+1}$, p^{k+1} for $k \geqslant 0$.

$$\frac{1}{\Delta t}(\tilde{\boldsymbol{u}} - \boldsymbol{u}^k) - \nu\nabla^2\tilde{\boldsymbol{u}} = \boldsymbol{F}(t^{k+1}), \quad \tilde{\boldsymbol{u}}|_\Gamma = 0 \tag{3.1.2}$$

$$\frac{1}{\Delta t}(\boldsymbol{u}^{k+1} - \tilde{\boldsymbol{u}}) + \nabla p^{k+1} = 0 \tag{3.1.3}$$

$$\nabla.\boldsymbol{u}^{k+1} = 0, \qquad \boldsymbol{u}^{k+1}.\boldsymbol{n}|_\Gamma = 0 \tag{3.1.4}$$

where ν is the kinematic viscosity and Γ is the boundary. Eqn. (3.1.3) is usually referred to as the projection step, or pressure-correction step. By taking the divergence of both sides of (3.1.3) and considering (3.1.4), we will solve the following Poisson's equation to compute p^{k+1}:

$$\nabla^2 p^{k+1} = \nabla.\tilde{\boldsymbol{u}}$$

There are two remarkable points about this approach [**20**]:

1. A Neumann boundary condition is enforced on the pressure for Eqn. (3.1.3). A numerical boundary layer resultes from this artificial Neumann boundary condition such that the scheme is not fully first-order for the velocity and pressure.

2. Using a more accurate discretizations of the time derivative in Eqns. (3.1.2)-(3.1.3) does not improve the overall accuracy of this scheme because it has an irreducible splitting error of order $O(\Delta t)$.

In the 1980s, several second order time-discrete versions of a projection method were proposed [**6**].

Some of these versions were motivated by the second order time-discrete semi-implicit forms:

$$\frac{\boldsymbol{u}^{n+1} - \boldsymbol{u}^n}{\Delta t} + \nabla p^{n+1/2} = -[(\boldsymbol{u}.\nabla)\boldsymbol{u}]^{n+1/2} + \frac{\nu}{2}\nabla^2(\boldsymbol{u}^{n+1} + \boldsymbol{u}^n) \tag{3.1.5}$$

$$\nabla.\boldsymbol{u}^{n+1} = 0 \tag{3.1.6}$$

$$\boldsymbol{u}^{n+1}|_{\partial\Omega} = \boldsymbol{u}_b^{n+1} \tag{3.1.7}$$

where $[(\boldsymbol{u}.\nabla)\boldsymbol{u}]^{n+1/2}$ is a second order approximation at time step $t = n + 1/2$ and $\boldsymbol{u}_b$ is a vector defining a boundary condition.

Eqns. (3.1.5)-(3.1.6) are hard to solve directly. Therefore, a fractional step may be used to approximate the solution of these two equations. To do so, an intermediate velocity variable $\boldsymbol{u}^*$ is introduced for solving an analog to Eqn. (3.1.5). There are three steps:

1. Step 1: Solve the following equation for the intermediate $\boldsymbol{u}^*$

$$\frac{\boldsymbol{u}^* - \boldsymbol{u}^n}{\Delta t} + \nabla q = -[(\boldsymbol{u}.\nabla)\boldsymbol{u}]^{n+1/2} + \frac{\nu}{2}\nabla^2(\boldsymbol{u}^* + \boldsymbol{u}^n) \tag{3.1.8}$$

where q is an approximation to $p^{n+1/2}$ and the boundary condition for $\boldsymbol{u}^*$ should be specified.

2. Step 2: The projection step

$$\boldsymbol{u}^* = \boldsymbol{u}^{n+1} + \Delta t \nabla \phi^{n+1} \tag{3.1.9}$$

$$\nabla.\boldsymbol{u}^{n+1} = 0 \tag{3.1.10}$$

with the Dirichlet boundary condition for $\boldsymbol{u}^*$ and the Neumann boundary condition for $\boldsymbol{u}^{n+1}$.

3. Step 3: Pressure-correction

$$p^{n+1/2} = q + L(\phi^{n+1}) \tag{3.1.11}$$

where L is a function of ϕ^{n+1}.

3.1.1. The selected projection scheme

In this work we use the Chorin's method with a slight modification [19]. The general problem to solve numerically and all the required steps are explained as follows:

We discretize the dimensionless Navier-Stokes equations given in the form of

$$\frac{\partial u}{\partial t} + \frac{\partial p}{\partial x} = -\frac{\partial u^2}{\partial x} - \frac{\partial (uv)}{\partial y} + \frac{1}{Re}\left(\frac{\partial^2 u}{\partial x^2} + \frac{\partial^2 u}{\partial y^2}\right) + F_x \tag{3.1.12}$$

$$\frac{\partial v}{\partial t} + \frac{\partial p}{\partial y} = -\frac{\partial (uv)}{\partial x} - \frac{\partial v^2}{\partial y} + \frac{1}{Re}\left(\frac{\partial^2 v}{\partial x^2} + \frac{\partial^2 v}{\partial y^2}\right) + F_y \tag{3.1.13}$$

$$\frac{\partial u}{\partial x} + \frac{\partial v}{\partial y} = 0, \tag{3.1.14}$$

on a rectangular domain $\Omega = [0 \times l_x] \times [0 \times l_y]$ where l_x and l_y are the dimensionless width and diameter of the channel, respectively.

For numerical approximations instead of considering u, v and p as the solutions of the Navier-Stokes equations we use U, V and P, respectively. Therefore, $U^n \approx u(n\Delta t, x, y)$ and $V^n \approx v(n\Delta t, x, y)$ are the velocity field components at the n^{th} time step satisfying

$$\frac{\partial U^n}{\partial x} + \frac{\partial V^n}{\partial y} = 0.$$

The solution at the time step $(n+1)$ is calculated in three steps, i.e., treating nonlinear terms step, an implicit viscosity step and a pressure correction step.

First, the nonlinear terms of the incompressible Navier-Stokes equations are treated

$$\frac{U^* - U^n}{\Delta t} = -\frac{\partial (U^n)^2}{\partial x} - \frac{\partial (U^n V^n)}{\partial y} - \tilde{K} + F_x \tag{3.1.15}$$

$$\frac{V^* - V^n}{\Delta t} = -\frac{\partial (U^n V^n)}{\partial x} - \frac{\partial (V^n)^2}{\partial y} + F_y \tag{3.1.16}$$

where $\tilde{K}$ is an imposed pressure gradient, F_x and F_y are the force density components exerted by the boundary of the clot on the fluid.

Second, after having obtained U^* and V^*, the viscosity terms, i.e., the intermediate velocity field (U^{**}, V^{**}) is introduced to improve the solutions U^* and V^* by solving the equations

$$\frac{U^{**} - U^*}{\Delta t} = \frac{1}{Re}\left(\frac{\partial^2 U^{**}}{\partial x^2} + \frac{\partial^2 U^{**}}{\partial y^2}\right) \tag{3.1.17}$$

$$\frac{V^{**} - V^*}{\Delta t} = \frac{1}{Re}\left(\frac{\partial^2 V^{**}}{\partial x^2} + \frac{\partial^2 V^{**}}{\partial y^2}\right) \tag{3.1.18}$$

with the boundary conditions for U^{**} and V^{**} chosen so that the boundary conditions for U^{n+1} and V^{n+1} are satisfied, at least approximately:

$$\begin{aligned}
U_N^{**} &:= U_{upper\,wall}^{**} = 0 \qquad & U_S^{**} &:= U_{lower\,wall}^{**} = 0 \\
U_W^{**} &:= U_{inflow}^{**}(y) = \frac{K}{2} y(y-1) + \frac{4K}{\pi^3} \sum_{j\ odd} \frac{1}{j^3} \sin(j\pi y) e^{-\frac{j^2\pi^2}{Re}(n+1)\Delta t} & & \\
\frac{\partial U_E^{**}}{\partial x} &:= \frac{\partial U_{outflow}^{**}}{\partial x} = 0 & & \\
V_N^{**} &:= V_{upper\,wall}^{**} = 0 \qquad & V_S^{**} &:= V_{lower\,wall}^{**} = 0 \\
V_W^{**} &:= V_{inflow}^{**} = 0 \qquad & V_E^{**} &:= V_{outflow}^{**} = 0
\end{aligned}$$

where the subscripts N, S, W and S denote the upper wall, the lower wall, inflow and outflow, respectively. K was already calculated and is equal to -12.

Finally, the intermediate velocity field is corrected:

$$\frac{U^{n+1} - U^{**}}{\Delta t} = -\frac{\partial \tilde{P}^{n+1}}{\partial x} \tag{3.1.19}$$

$$\frac{V^{n+1} - V^{**}}{\Delta t} = -\frac{\partial \tilde{P}^{n+1}}{\partial y} \tag{3.1.20}$$

where $\tilde{P}^{n+1}$ is an approximation of $\tilde{p}((n+1)\Delta t, x, y)$. Since in Eqns. (3.1.19)-(3.1.20) the excess pressure is at time step $(n+1)$, it should be treated implicitly. Enforcing incompressibility at

each time step means that, by taking the derivative of both sides of (3.1.19) with respect to x and (3.1.20) with respect to y we end up with

$$-\frac{1}{\Delta t}\frac{\partial U^{**}}{\partial x} = -\frac{\partial^2 \tilde{P}^{n+1}}{\partial x^2} \tag{3.1.21}$$

$$-\frac{1}{\Delta t}\frac{\partial V^{**}}{\partial y} = -\frac{\partial^2 \tilde{P}^{n+1}}{\partial y^2} \tag{3.1.22}$$

$$\Rightarrow \quad -(\frac{1}{\Delta t}\frac{\partial U^{**}}{\partial x} + \frac{1}{\Delta t}\frac{\partial V^{**}}{\partial y}) = -(\frac{\partial^2 \tilde{P}^{n+1}}{\partial x^2} + \frac{\partial^2 \tilde{P}^{n+1}}{\partial y^2}) \tag{3.1.23}$$

Taking $F^n = -(\frac{1}{\Delta t}\frac{\partial U^{**}}{\partial x} + \frac{1}{\Delta t}\frac{\partial V^{**}}{\partial y})$, therefore, we solve Poisson's equation

$$-\Delta \tilde{P}^{n+1} = F^n$$

with the following boundary conditions for $\tilde{P}^{n+1}$ chosen so that the boundary conditions for U^{n+1} and V^{n+1} given by (3.1.19)-(3.1.20) and the pressure (2.1.48) are satisfied

$$\begin{aligned}
&\frac{\partial \tilde{P}^{n+1}}{\partial x} = 0 && \text{on inflow}\\
&\tilde{P}^{n+1} = 0 && \text{on outflow}\\
&\frac{\partial \tilde{P}^{n+1}}{\partial y} = 0 && \text{on the upper and lower walls}
\end{aligned}$$

Having found $\tilde{P}^{n+1}$, we compute $\frac{\partial}{\partial x}(\tilde{P}^{n+1})$ and $\frac{\partial}{\partial y}(\tilde{P}^{n+1})$ and substitute them in (3.1.19) and (3.1.20), respectively, to update the velocity field

$$(U^{n+1}\,,\, V^{n+1}) = (U^{**} - \Delta t\frac{\partial \tilde{P}^{n+1}}{\partial x}\,,\, V^{**} - \Delta t\frac{\partial \tilde{P}^{n+1}}{\partial y})$$

Algorithm 1 The projection scheme algorithm

Treat nonlinear terms:
1: Solve the equation $\frac{\boldsymbol{u}^* - \boldsymbol{u}^n}{\Delta t} = -(\boldsymbol{u}^n.\nabla)\boldsymbol{u}^n$ for $\boldsymbol{u}^*$
Implicit Viscosity:
2: Solve the implicit equation $\frac{\boldsymbol{u}^{**} - \boldsymbol{u}^*}{\Delta t} = \frac{1}{Re}(\nabla^2 \boldsymbol{u}^{**})$ for $\boldsymbol{u}^*$
Pressure Correction
3: Applying the Helmholtz-Hodge decomposition on $\frac{\boldsymbol{u}^{n+1} - \boldsymbol{u}^{**}}{\Delta t} = -\nabla \tilde{p}^{n+1}$
4: $-\nabla^2 \tilde{p}^{n+1} = -\frac{1}{\Delta t}\nabla.\boldsymbol{u}^{**}$

3.1.2. Spatial discretization

In order to solve Eqns. (3.1.17) and (3.1.18), we should discretize them spatially on a suitable mesh. For the first derivatives as well as the second derivatives, we use central finite differences. Using a regular grid (collocated grid), all the variables are located on the same point of the grid and this leads to spurious pressure mode instabilities, when the pressure term is approximated by central differencing [**11**] because of the coupling between the pressure and the velocity.

In order to avoid this instability we use a staggered grid. This grid is divided into cells such that $\tilde{P}^{n+1}$ is computed on the cell centers and the intermediate velocities (U^{**} and V^{**}) are computed on the vertical and horizontal cell boundaries, respectively [**31**, **40**].

Fig. 3.2 shows a staggered grid in which for each cell, the center represents $\tilde{P}^{n+1}$, the center of left side represents U^{**} and the lower side center represents V^{**}.

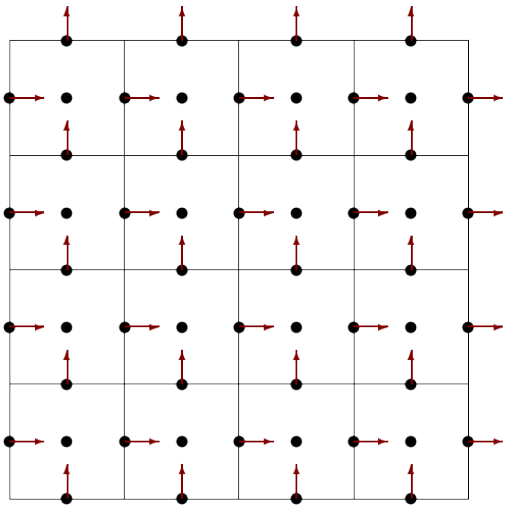

FIGURE 3.2. A staggered grid; horizontal and vertical arrows represent the intermediates velocities U^{**} and V^{**}, respectively.

In our problem, according to the boundary conditions, these three fields should be computed on the interior points. Additionally, U^{**} should be computed on outflow points. The number of unknowns to determine for each field is given in Table 3.I.

TABLE 3.I. Pressure and velocity fields sizes

Field	Grid points
Pressure $\tilde{P}^{n+1}$	$n_x \times n_y$
Velocity component U^{**}	$n_x \times n_y$
Velocity component V^{**}	$n_x \times (n_y - 1)$

n_x and n_y are the number of the cells in each row and each column of the rectangular domain, respectively. Therefore, the length and height of each cell are defined by $h_x = \frac{l_x}{n_x}$ and $h_x = \frac{l_y}{n_y}$, respectively.

Eqns. (3.1.17)-(3.1.20) are discretized at interior and outflow points for U^{**} and at interior points for V^{**} and $\tilde{P}^{n+1}$. The second derivatives are approximated by centred finite differences at a grid point related to the corresponding field. For example, to approximate the second derivative of $U^{**}_{i+1/2,j}$ with respect to x we have

$$\frac{\partial^2 U^{**}_{i+1/2,j}}{\partial x^2} = \frac{U^{**}_{i-1/2,j} - 2U^{**}_{i+1/2,j} + U^{**}_{i+3/2,j}}{h_x^2} \qquad i = 1, \ldots, n_x, \ j = 1, \ldots, n_y$$

If $i = 1$, $U^{**}_{i-1/2,j}$ is located on inflow and if $i = n_x$, $U_{nx+1/2}$ is located on a so-called ghost cell. Ghost cells appear on the right side of outflow, on the top of the upper wall and on the bottom of the lower wall and are added in order that the boundary conditions for U^{**}, V^{**} and $\tilde{P}^{n+1}$ may be satisfied. See Fig. 3.3, [40]. We describe how this is done in the remainder of this section.

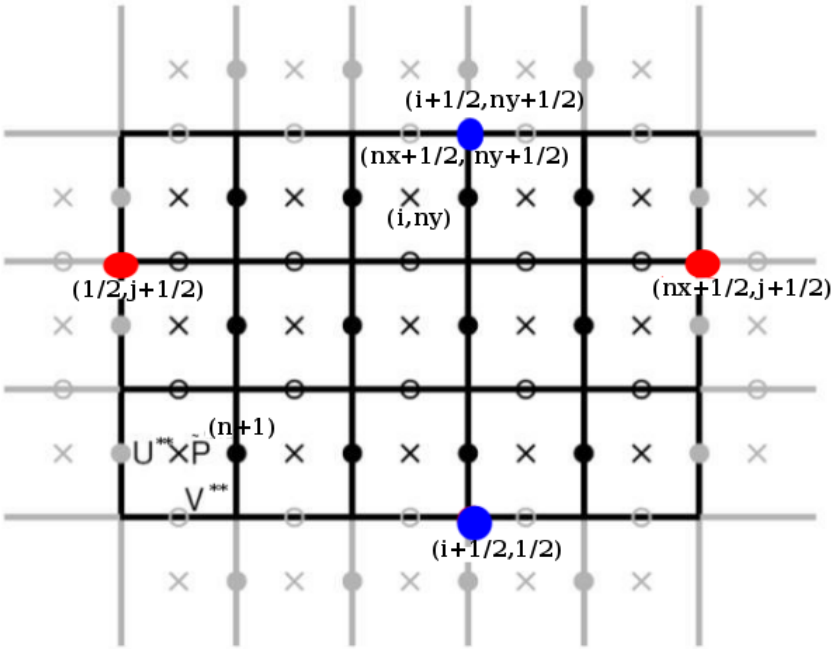

FIGURE 3.3. A staggered grid with the boundary cell and ghost cells (gray cells);

The intermediate velocity $U^{**}_{1/2,j}$ at inflow is prescribed directly. The homogeneous Neumann boundary condition $\frac{\partial U^{**}_{nx+1/2,j}}{\partial x} = 0$ on outflow can be treated as:

$$\frac{U^{**}_{ghost} - U^{**}_{n_x-1/2}}{2h_x} = 0 \qquad \Rightarrow \qquad U^{**}_{ghost} = U^{**}_{n_x-1/2} \quad \text{(outflow ghost cell)}$$

resulting in a modification to the discretization of $\frac{\partial^2 U^{**}}{\partial x^2}$ as follows:

$$\frac{U^{**}_{n_x-1/2,j} - 2U^{**}_{n_x+1/2,j} + U^{**}_{ghost,j}}{h_x^2} = \frac{U^{**}_{n_x-1/2,j} - 3U^{**}_{n_x+1/2,j}}{h_x^2}$$

Similarly, on the lower and upper walls we prescribe the values for V^{**} directly. Therefore, the discretized $\frac{\partial^2 V^{**}}{\partial y^2}$ for $j = 1$ and $j = n_y$ is

$$\begin{aligned}
&V^{**}_{i,1/2} = V^{**}_{i,lower\ wall} = 0 \\
&V^{**}_{i,ny+1/2} = V^{**}_{i,upper\ wall} = 0 \\
&\frac{V^{**}_{i,1/2} - 2V^{**}_{i,3/2} + V^{**}_{i,5/2}}{h_y^2} = \frac{-2V^{**}_{i,3/2} + V^{**}_{i,5/2}}{h_y^2} \\
&\frac{V^{**}_{i,n_y-3/2} - 2V^{**}_{i,n_y-1/2} + V^{**}_{i,n_y+1/2}}{h_y^2} = \frac{V^{**}_{i,n_y-3/2} - 2V^{**}_{i,n_y-1/2}}{h_y^2}
\end{aligned}$$

For the values of U^{**} on the upper and lower walls that lie between grid points of U^{**} and artificial ghost points, we take the average of the two points below and above the boundary (Fig. 3.3).

Since $U^{**}_{i+1/2,n_y+1/2} = U^{**}_{i+1/2,1/2} = 0$, the discretized $\frac{\partial^2 U^{**}}{\partial y^2}$ is:

$$U^{**}_{i+1/2,n_y+1/2} = \frac{U^{**}_{i+1/2,ghost} + U_{i+1/2,n_y}}{2} = 0$$

where $U^{**}_{i+1/2,ghost}$ is the upper wall neighboring ghost cell,

$$\begin{aligned}
&\Rightarrow \quad U^{**}_{i+1/2,ghost} = -U^{**}_{i+1/2,n_y} \\
&\Rightarrow \quad \frac{U^{**}_{i+1/2,n_y-1} - 2U^{**}_{i+1/2,n_y} + U^{**}_{i+1/2,ghost}}{h_y^2} = \frac{U^{**}_{i+1/2,n_y-1} - 3U^{**}_{i+1/2,n_y}}{h_y^2}.
\end{aligned}$$

Moreover,

$$U^{**}_{i+1/2,1/2} = \frac{U^{**}_{i+1/2,ghost} + U^{**}_{i+1/2,1}}{2} = 0$$

where $U^{**}_{i+1/2,ghost}$ is the lower wall neighboring ghost cell,

$$\begin{aligned}
&\Rightarrow \quad U^{**}_{i+1/2,ghost} = -U^{**}_{i,1} \\
&\Rightarrow \quad \frac{U^{**}_{i+1/2,ghost} - 2U^{**}_{i+1/2,1} + U^{**}_{i+1/2,2}}{h_y^2} = \frac{-3U^{**}_{i+1/2,1} + U^{**}_{i+1/2,2}}{h_y^2}
\end{aligned}$$

On inflow and outflow $V^{**}_{1/2,j+1/2} = V_{n_x+1/2,j+1/2}{}^{**} = 0$, therefore we have (Fig. 3.3):

$$V^{**}_{1/2,j+1/2} = \frac{V^{**}_{ghost,j+1/2} + V^{**}_{1,j+1/2}}{2} = 0$$

where $V^{**}_{ghost,j+1/2}$ is the inflow neighboring ghost cell,

$$\begin{aligned} \Rightarrow \quad & V^{**}_{ghost,j+1/2} = -V^{**}_{1,j+1/2} \\ \Rightarrow \quad & \frac{V^{**}_{ghost,j+1/2} - 2V^{**}_{1,j+1/2} + V^{**}_{2,j+1/2}}{h_x^2} = \frac{-3V^{**}_{1,j+1/2} + V^{**}_{2,j+1/2}}{h_x^2}. \end{aligned}$$

Moreover,

$$V^{**}_{n_x+1/2,j+1/2} = \frac{V^{**}_{n_x+1/2,j+1/2} + V^{**}_{ghost,j+1/2}}{2} = 0$$

where $V^{**}_{ghost,j+1/2}$ is the outflow neighboring ghost cell,

$$\begin{aligned} \Rightarrow \quad & V^{**}_{ghost,j+1/2} = -V^{**}_{n_x,j+1/2} \\ \Rightarrow \quad & \frac{V^{**}_{n_x-1,j+1/2} - 2V^{**}_{n_x,j+1/2} + V^{**}_{ghost,j+1/2}}{h_x^2} = \frac{V^{**}_{n_x-1,j+1/2} - 3V^{**}_{n_x,j+1/2}}{h_x^2} \end{aligned}$$

Finally, the boundary conditions $\frac{\partial \tilde{P}^{n+1}}{\partial x} = 0$ on inflow, $\tilde{P}^{n+1} = 0$ on outflow and $\frac{\partial \tilde{P}^{n+1}}{\partial y} = 0$ on the upper and lower walls are used in the discretization at certain points of $\frac{\partial^2 \tilde{P}^{n+1}}{\partial x^2}$ and $\frac{\partial^2 \tilde{P}^{n+1}}{\partial y^2}$ since Poisson's equation is solved at all interior points.

A centred difference approximation to $\frac{\partial \tilde{P}^{n+1}}{\partial x} = 0$ on inflow is written as

$$\frac{\tilde{P}^{n+1}_{ghost,j+1/2} - \tilde{P}^{n+1}_{1,j+1/2}}{h_x} = 0$$

where $\tilde{P}^{n+1}_{ghost,j+1/2}$ is the inflow neighboring ghost cell. Therefore, $\tilde{P}^{n+1}_{ghost,j+1/2} = \tilde{P}^{n+1}_{1,j+1/2}$ results in

$$\frac{\tilde{P}^{n+1}_{ghost,j+1/2} - 2\tilde{P}^{n+1}_{1,j+1/2} + \tilde{P}^{n+1}_{2,j+1/2}}{h_x^2} = \frac{-\tilde{P}^{n+1}_{1,j+1/2} + \tilde{P}^{n+1}_{2,j+1/2}}{h_x^2}$$

Similarly, a centred difference approximation to $\frac{\partial \tilde{P}^{n+1}}{\partial y} = 0$ on the upper wall is

$$\frac{\tilde{P}^{n+1}_{i,ghost} - \tilde{P}^{n+1}_{i,n_y}}{h_y} = 0$$

where $\tilde{P}^{n+1}_{i,ghost}$ is the upper wall neighboring ghost cell. Therefore, $\tilde{P}^{n+1}_{i,ghost} = \tilde{P}^{n+1}_{i,n_y}$ gives us

$$\frac{\tilde{P}^{n+1}_{i,n_y-1} - 2\tilde{P}^{n+1}_{i,n_y} + \tilde{P}^{n+1}_{i,ghost}}{h_y^2} = \frac{\tilde{P}^{n+1}_{i,n_y-1} - \tilde{P}^{n+1}_{i,n_y}}{h_y^2}$$

The Neumann boundary condition $\frac{\partial \tilde{P}^{n+1}}{\partial y} = 0$ on the lower wall is discretized using a centred finite difference as

$$\frac{\tilde{P}^{n+1}_{i,ghost} - \tilde{P}_{i,1}}{h_y} = 0$$

where $\tilde{P}_{i,ghost}$ is the lower wall neighboring ghost cell. Therefore,

$$\frac{\tilde{P}^{n+1}_{i,ghost} - 2\tilde{P}^{n+1}_{i,1} + \tilde{P}^{n+1}_{i,2}}{h_y^2} = \frac{-\tilde{P}^{n+1}_{i,1} + \tilde{P}^{n+1}_{i,2}}{h_y^2}$$

And lastly, $\tilde{P}^{n+1} = 0$ on outfolow which can be approximated by

$$\frac{\tilde{P}^{n+1}_{ghost,j} + \tilde{P}^{n+1}_{n_x,j}}{2} = 0$$

where $\tilde{P}^{n+1}_{ghost,j}$ is the outflow neighboring ghost cell.

Therefore, $\tilde{P}^{n+1}_{ghost,j} = -\tilde{P}^{n+1}_{n_x,j}$ results in

$$\frac{\tilde{P}^{n+1}_{n_x-1,j} - 2\tilde{P}^{n+1}_{n_x,j} + \tilde{P}^{n+1}_{ghost,j}}{h_x^2} = \frac{\tilde{P}^{n+1}_{n_x-1,j} - 3\tilde{P}^{n+1}_{n_x,j}}{h_x^2}$$

3.1.2.1. *The matrix representations of the intermediate velocities and the excess pressure*

In order to solve Eqns. (3.1.17) and (3.1.18) for U^{**} and V^{**}, we bring all the unknowns on one side and the knowns and the boundary conditions on the other side

$$U^{**}_{i+1/2,j} - \frac{\Delta t}{Re}\Big(\frac{U^{**}_{i-1/2,j} - 2U^{**}_{i+1/2,j} + U^{**}_{i+3/2,j}}{h_x^2} + \frac{U^{**}_{i,j-1/2} - 2U^{**}_{i,j+1/2} + U^{**}_{i,j+3/2}}{h_y^2}\Big) = U^* + U_{bc} \tag{3.1.24}$$

where U_{bc} is the known value of U^{**} and U^* is given by (3.1.15).

$$V^{**}_{i,j+1/2} - \frac{\Delta t}{Re}\Big(\frac{V^{**}_{i-1/2,j} - 2V^{**}_{i+1/2,j} + V^{**}_{i+3/2,j}}{h_x^2} + \frac{V^{**}_{i,j-1/2} - 2V^{**}_{i,j+1/2} + V^{**}_{i,j+3/2}}{h_y^2}\Big) = V^* + V_{bc} \tag{3.1.25}$$

where V_{bc} is the known value of V^{**} and V^{*} is given by (3.1.16).

Therefore, $\frac{\partial^2 U^{**}}{\partial x^2}$ and $\frac{\partial^2 U^{**}}{\partial y^2}$ on the left-hand side of (3.1.24) have the sparse matrix forms, respectively as follows

$$\begin{bmatrix} -2 & 1 & & & & \\ 1 & -2 & 1 & & & \\ & \ddots & \ddots & \ddots & & \\ & & 1 & -2 & 1 & \\ & & & 2 & -2 & \end{bmatrix} \tag{3.1.26}$$

and

$$\begin{bmatrix} -3 & 1 & & & & \\ 1 & -2 & 1 & & & \\ & \ddots & \ddots & \ddots & & \\ & & 1 & -2 & 1 & \\ & & & 1 & -3 & \end{bmatrix} \tag{3.1.27}$$

The sparse coefficient matrices for $\frac{\partial^2 V^{**}}{\partial x^2}$ and $\frac{\partial^2 V^{**}}{\partial y^2}$ are

$$\begin{bmatrix} -3 & 1 & & & & \\ 1 & -2 & 1 & & & \\ & \ddots & \ddots & \ddots & & \\ & & 1 & -2 & 1 & \\ & & & 1 & -3 & \end{bmatrix} \tag{3.1.28}$$

and

$$\begin{bmatrix} -2 & 1 & & & & \\ 1 & -2 & 1 & & & \\ & \ddots & \ddots & \ddots & & \\ & & 1 & -2 & 1 & \\ & & & 1 & -2 & \end{bmatrix}, \tag{3.1.29}$$

respectively. Having solved Eqns. (3.1.17) and (3.1.18) we use U^{**} and V^{**} in (3.1.21) and (3.1.22). The sparse matrices representing $\frac{\partial^2 \tilde{P}^{n+1}}{\partial x^2}$ and $\frac{\partial^2 \tilde{P}^{n+1}}{\partial y^2}$ have the following forms.

$$\begin{bmatrix} -1 & 1 & & & & \\ 1 & -2 & 1 & & & \\ & \ddots & \ddots & \ddots & & \\ & & 1 & -2 & 1 & \\ & & & 1 & -3 \end{bmatrix} \tag{3.1.30}$$

and

$$\begin{bmatrix} -2 & 1 & & & & \\ 1 & -2 & 1 & & & \\ & \ddots & \ddots & \ddots & & \\ & & 1 & -2 & 1 & \\ & & & 1 & -2 \end{bmatrix} \tag{3.1.31}$$

respectively.

3.2. THE IMMERSED BOUNDARY METHOD

For a viscous incompressible fluid in a region containing an immersed boundary, Peskin in 1972 introduced the first version of the immersed boundary method to study the flow behavior in the presence of the forces exerted by the boundary on the fluid, [34]. In the non-dimensionalized Navier-Stokes equations given by (3.1.12)-(3.1.13), $\boldsymbol{F} = (F_x, F_y)$ is the external force exerted by the immersed boundary on the surrounding fluid. Assume a small length of the immersed boundary a force $\boldsymbol{f}(s,t)ds$ at time t is exerted on the surrounding fluid (s is a Lagrangian variable). The total force is then given by

$$\boldsymbol{F}(\boldsymbol{x},t) = \iint \boldsymbol{f}(s,t)\delta(\|\boldsymbol{x} - \boldsymbol{X}(s,t)\|)\, ds \tag{3.2.1}$$

where δ indicates a two-dimensional Dirac delta function, $\boldsymbol{x}$ is a point in the Cartesian grid and $\boldsymbol{X}$ is the coordinate of a Lagrangian point on the immersed boundary. In a discrete representation the function δ may be approximated with a function $D(\boldsymbol{X}_k)$ such that $\boldsymbol{X}_k$ belongs to the immersed boundary

$$D(\boldsymbol{X}_k) = \begin{cases} \frac{1}{16h^2}(2 - |\alpha - x|)(2 - |\beta - y|), & |\alpha - x| \leqslant 2 \text{ and } |\beta - y| \leqslant 2 \\ 0, & \text{otherwise} \end{cases}$$

where $\boldsymbol{X}_k = (\alpha h, \beta h)$ is a point on the Lagrangian mesh, $\boldsymbol{x} = (x, y)$ is a Cartesian mesh point and h is the mesh width on a square mesh. Some examples of semidiscrete analogs of this δ function are given in Fig. 3.4.

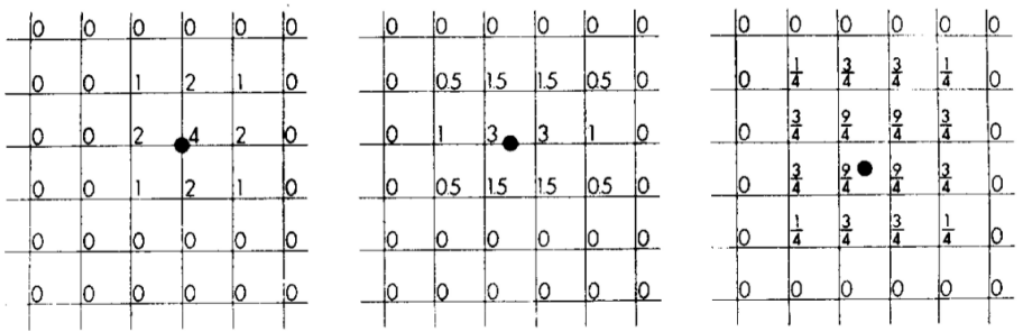

FIGURE 3.4. Semidiscrete analog of the δ function: three typical cases (the factor $1/16h^2$ has been omitted). The coefficients shown provide the linkage between the boundary points and the fluid mesh [34]

A few years later, in 1977, Peskin [35] introduced an improved numerical representation of the function δ (Fig. 3.5)

$$D(\boldsymbol{X}_k) = d(x_k - x)d(y_k - y)$$

where

$$d(r) = \begin{cases} \frac{1}{4}h(1 + \cos(\pi r/2h)), & \text{if } |r| < 2h \\ 0 & \text{if } |r| \geqslant 2h \end{cases}$$

where $\boldsymbol{X}_k = (x_k, y_k)$ is a Lagrangian grid point, (x, y) is a Cartesian grid point and h is the mesh width on a squared grid.

Tu and Peskin [45] compared the stability properties of three numerical methods for computing the boundary force in the presence of an elastic immersed boundary. The numerical approximation δ_h to the δ function used for all of them is the one introduced in [35].

The first method is an explicit method which is not always stable and when we have a big time step for the membrane position update the boundary will explode. To compute the updated positions of the boundary points $\boldsymbol{X}^{n+1}$ at time step $(n + 1)$ given $\boldsymbol{X}^n$, the force density $\boldsymbol{f}_k^n$ exerted by each point of the boundary $\boldsymbol{X}_k$ should be evaluated first. Then, the δ_h function is used to calculate the force density $\boldsymbol{F}_{ij}^n$ on all the computational grid points

$$\boldsymbol{F}_{ij}^n = \sum_k \boldsymbol{f}_k^n \delta_h\Big(\boldsymbol{x}_{ij} - \boldsymbol{X}_k^n\Big)\delta s$$

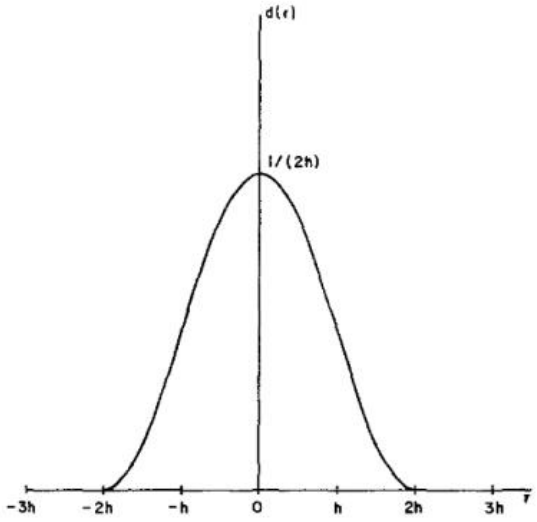

FIGURE 3.5. Numerical representation of the function δ [35]

where k runs over all the particles on the boundary, $\boldsymbol{x}_{ij}$ is a grid point, $\boldsymbol{X}_k^n$ is a boundary point at the time step n and Δs is the distance between two successive boundary particles.

Next, having solved the velocity $\boldsymbol{u}_{ij}^n$ on the grid points in the Navier-Stokes equations, they use the δ_h function again to interpolate the velocity on the boundary points $\boldsymbol{U}_k^n$

$$\boldsymbol{U}_k^n = \sum_{ij} \boldsymbol{u}_{ij}^n \delta_h\Big(\boldsymbol{x}_{ij} - \boldsymbol{X}_k^n\Big)h^2.$$

Finally, the boundary positions are updated using

$$\boldsymbol{X}_k^{n+1} = \boldsymbol{X}_k^n + \Delta t \boldsymbol{U}_k^n.$$

The second method used the approximate-implicit method which is similar to the first one except that in order to avoid the numerical instability the force density was calculated implicitly. The following system of equations was used to calculate the force density $\boldsymbol{f}_k$ exerted by each boundary particle.

$$\boldsymbol{X}_k^{n+1,*} = \boldsymbol{X}_k^n + \Delta t \lambda \boldsymbol{f}_k\Big(\boldsymbol{X}_1^{n+1,*}, \boldsymbol{X}_2^{n+1,*}, \ldots, \boldsymbol{X}_{N_b}^{n+1,*}\Big),$$

where $\boldsymbol{X}_1^{n+1.*}$, $\boldsymbol{X}_2^{n+1.*}$, $\ldots$, $\boldsymbol{X}_{N_b}^{n+1.*}$ are the intermediate boundary positions, λ is the magnitude of the velocity induced at a point by a unit force applied to that point. For more details see [45]

An implicit method was the third approach in which they calculated the boundary force with respect to the unknown configuration at the end of the time step. This method uses the fundamental solution of the Stokes equations to compute the influence of one boundary point on another [45]. Having found the velocity $\boldsymbol{u}_{ij}$ at each grid point, an implicit method was used to compute the force

density

$$\boldsymbol{X}_k^{n+1} = \boldsymbol{X}_k^n + \Delta t h^2 \sum_{ij} \boldsymbol{u}_{ij}^{n+1} \delta_h\Big(\boldsymbol{x}_{ij} - \boldsymbol{X}_k^n\Big).$$

where $\boldsymbol{X}_k^{n+1}$ is an updated boundary position at the time step $(n+1)$, h is the mesh width on a square grid and $\boldsymbol{x}_{ij}$ is a grid point.

The reason for calling this the implicit method is because the boundary force was computed from $\boldsymbol{X}_k^{n+1}$ [45]. Once the updated boundary force exerted by each boundary point $\boldsymbol{f}_k^{n+1}$ was calculated, the updated boundary points were found fromm

$$\boldsymbol{X}_k^{n+1} = \boldsymbol{X}_k^0 + \Delta t\, \Delta s \tilde{\boldsymbol{G}} \boldsymbol{f}_k^{n+1};$$

where $\boldsymbol{G}$ is the discrete Green's function of the Stokes equations on a periodic domain (further details can be found in [45]).

This method in comparison to the other ones had the best stability properties.

Roma *et al.*, [38] suggested an adaptive mesh refinement technique and defined the discrete approximated δ function as follows

$$\delta_h^2(\boldsymbol{x} = \boldsymbol{x}_0) = \delta_h^1(x - x_0)\delta_h^1(y - y_0)$$

where $\boldsymbol{x} = (x, y)$ is a point on the immersed boundary, $\boldsymbol{x}_0 = (x_0, y_0)$ is a Cartesian mesh point, h is the mesh width on a square grid and ϕ is defined as

$$\phi(r) = \begin{cases} \frac{1}{6}(5 - 3|r| - \sqrt{-3(1 - r^2 + 1)}), & 0.5 \leqslant |r| \leqslant 1.5 \\ \frac{1}{3}(1 + \sqrt{-3 + r^2 + 1}), & |r| \leqslant 0.5 \\ 0, & \text{otherwise} \end{cases}$$

where $r = (x - x_0)/h$. $\delta_h^1(x - x_0) = \frac{1}{h}\phi\Big(\frac{x - x_0}{h}\Big)$.

This method was tested for a two-dimensional problem but no significant difference was found between the solution given by the locally refined mesh and a uniform mesh.

Other discrete δ functions have been used or introduced (Fig. 3.6).

In all the following functions, r is the distance between an Eulerian grid point and a Lagrangian grid point and h is the mesh width. Saiki [39] used the following function:

$$\delta(r) \approx d_h(r) = \frac{1}{h} \begin{cases} \frac{1}{4h^2}(2h + r), & \text{if } r \leqslant 2h \\ 0, & \text{otherwise.} \end{cases}$$

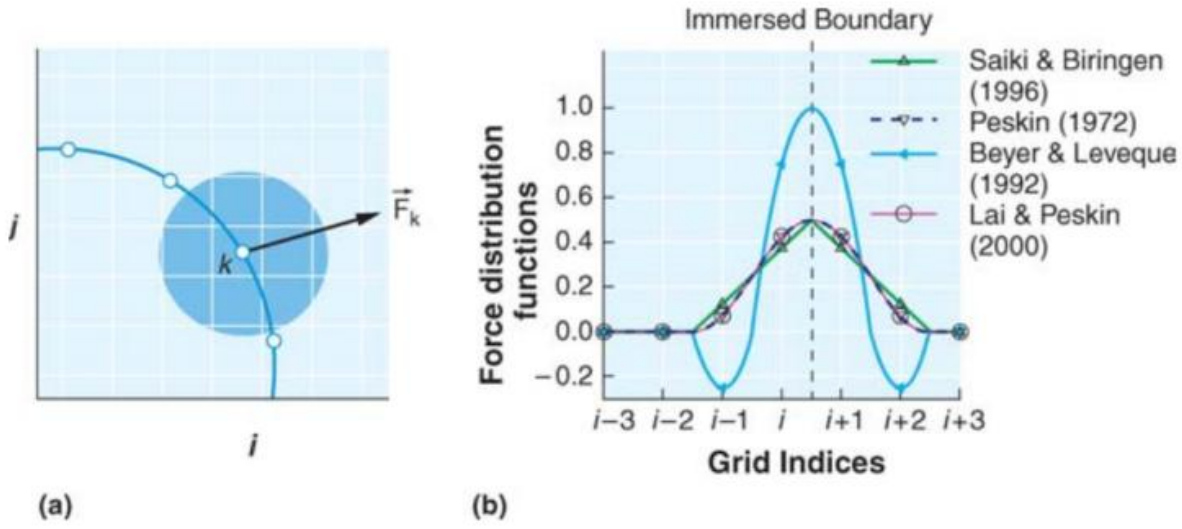

FIGURE 3.6. (a) The force $\boldsymbol{F}_k$ exerted from Lagrangian boundary point to surrounding fluid. (b) Various distribution functions [28].

If there are no discontinuities where the force is exerted, the simple discrete functions used by [35] and [39] are second and first order accurate, respectively [4]. Beyer and Leveque [4] introduced a more general discrete δ function and gave an interpretation for this function by extrapolating it linearly on both sides of the discontinuity associated with a convex combination of two one-sided extrapolations.

$$\delta(r) \approx d_h(r) = \begin{cases} 1 - (\frac{r}{h})^2, & \text{if } r \leqslant h \\ 2 - 3\frac{r}{h} + (\frac{r}{h})^2, & \text{if } h \leqslant r \leqslant 2h \\ 0, & \text{otherwise.} \end{cases}$$

A formally second-order accurate immersed boundary method was presented by Lai and Peskin [25] in which they used an explicit scheme for an immersed boundary method in which the boundary force is computed in the beginning of the time step and then the Navier-Stokes equations with the computed density force at time step n are solved to update the velocity field. The discrete delta function is defined as follows

$$\delta(\boldsymbol{x}) = d_h(x)d_h(y)$$

where $\boldsymbol{x} = (x, y)$ is an Eulerian variable and

$$d_h(r) = \begin{cases} \frac{1}{8h}(3 - 2|\frac{r}{h}| + \sqrt{1 + 4|\frac{r}{h}| - 4(\frac{r}{h})^2}), & \text{if } |r| \leqslant h \\ \frac{1}{8h}(5 - 2|\frac{r}{h}| - \sqrt{-7 + 12|\frac{r}{h}| - 4(\frac{r}{h})^2}), & \text{if } h \leqslant |r| \leqslant 2h \\ 0, & \text{otherwise.} \end{cases}$$

To study blood behavior everywhere including around the clot in a rectangular channel, the immersed boundary method has been deployed which is both a mathematical formulation and a numerical scheme.

In this work, the nondimensionalized net force density $\boldsymbol{F}$ exerted by the immersed boundary on the surrounding fluid is given by (2.2.20).

The reason for using a Dirac delta function in (2.2.20) is incompatibility of the location of immersed boundary with the points of the Cartesian mesh.

3.2.1. Our choice of delta function

For computing the net force given by (2.2.17) and resulting from (2.2.20), we need an approximation to the δ-function. The approximation used here is two-dimensional version of the one introduced by Peskin [36].

Suppose δ_h is the approximation to the δ-function so that $\delta_h \to \delta$ as $h \to 0$. A δ_h-function with such a property is defined as follows

$$\delta_h(x, y) = \frac{1}{h^2}\phi(\frac{x}{h})\phi(\frac{y}{h})$$

where h is the meshwidth and L is a characteristic length. The single-variable function $\phi(r)$, where r is a general real variable that can be taken as x/h or y/h, is a continuous function defined as follows

$$\phi(r) = \begin{cases} 0, & r \leq -2 \\ \frac{1}{8}\Big(5 + 2r - \sqrt{-7 - 12r - 4r^2}\Big), & -2 \leq r \leq -1 \\ \frac{1}{8}\Big(3 + 2r + \sqrt{1 - 4r - 4r^2}\Big), & -1 \leq r \leq 0 \\ \frac{1}{8}\Big(3 - 2r + \sqrt{1 + 4r - 4r^2}\Big), & 0 \leq r \leq 1 \\ \frac{1}{8}\Big(5 - 2r - \sqrt{-7 + 12r - 4r^2}, & 1 \leq r \leq 2 \\ 0, & 2 \leq r \end{cases}$$

From the definition of the function $\phi(r)$, the support of this function is in the interval $[-2, 2]$. More precisely, for the variables x and y the function δ_h has the support on $x, y \in [-2h, 2h]$.

Hence, the dimensionless function δ_h^* is δ_h multiplied by L^2. Therefore, by applying the nondimensionalized δ_h^* function in (2.2.20) the stress is distributed smoothly. In the numerical scheme, the number of grid points affected by the delta function depends on where the δ-function is positioned in the grid, but the strong point about the function ϕ is that it can easily include or exclude these grid points. We should bear in our mind that each boundary point of the clot is considered as a reference point (Fig. 3.7). Consequently, x and y are defined as $|x_{ij} - X_k|$ and $|y_{ij} - Y_k|$, respectively,

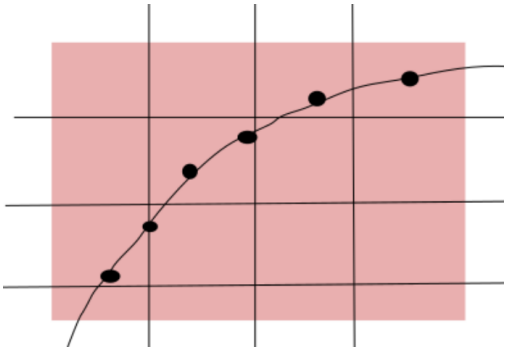

FIGURE 3.7. The clot boundary points in a Cartesian mesh.

where x_{ij} and y_{ij} are the coordinates of each grid point and X_k and Y_k are the coordinates of each boundary point on the clot. There are other choices for $\phi(r)$ such as $\exp(-r^2/2)$ or $\sin(r)/r$, but these would lead to large computational cost.

From now on, we are able to evaluate the exerted force $\boldsymbol{F} = (F_x, F_y)$ by the clot on the surrounding fluid, i.e., at each of the U^{**} and V^{**} grid points. Let F_x be the evaluated component at the U^{**} grid points and F_y be the evaluated component at the V^{**} grid points

$$F_x = \sum_i F_i^x \, \delta_h(|x^{U^*} - X_i|, |y^{U^*} - Y_i|) \tag{3.2.2}$$

$$F_y = \sum_i F_i^y \, \delta_h(|x^{V^*} - X_i|, |y^{V^*} - Y_i|) \tag{3.2.3}$$

where (F_i^x, F_i^y) are the components of F_i given by (2.2.20), (x^{U^*}, y^{U^*}) is a U^* grid point and (x^{V^*}, y^{V^*}) is a V^* grid point.

3.3. UPDATING THE POSITION OF THE POINTS INSIDE AND ON THE CLOT BOUNDARY

The position of the clot boundary is updated after having updated the velocities

$U^n \approx U(n\Delta t, x, y)$ and $V^n \approx V(n\Delta t, x, y)$ at every time step. To find the updated position, we should evaluate the fluid velocity at the boundary points. Assume $\boldsymbol{X}$ is the position of a particle

on the immersed boundary Let $\boldsymbol{u}_{\boldsymbol{X}}^n = \boldsymbol{u}(n\Delta t, \boldsymbol{X})$ be the numerical approximation to the fluid velocity at the boundary point $\boldsymbol{X}$ at time step $t = n\Delta t$ and suppose $\boldsymbol{u}_{\boldsymbol{X}}^n = (u_{\boldsymbol{X}}^n, v_{\boldsymbol{X}}^n)$. Then, we can linearly interpolate $u_{\boldsymbol{X}}^n$ using the U^n grid points which lie on the cell containing $\boldsymbol{X}$. Similarly, $v_{\boldsymbol{X}}^n$ can be linearly interpolated using the two V^n grid points which lie on the cell containing $\boldsymbol{X}$. Therefore,

$$u_{\boldsymbol{X}} = \frac{d_2 U_{i-1/2,j}^n + d_1 U_{i+1/2,j}^n}{h_x}$$
$$v_{\boldsymbol{X}} = \frac{d_3 V_{i,j-1/2}^n + d_4 V_{i,j+1/2}^n}{h_y}$$

where $d_1 + d_2 = h_x$ and $d_3 + d_4 = h_y$ (see Fig. 3.8).

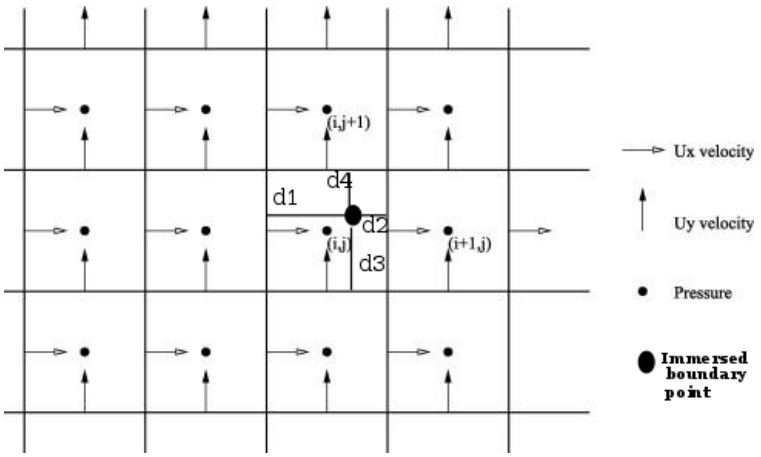

FIGURE 3.8. The position of an immersed boundary point with respect to the mesh grid.

Using the modified Euler method will help us to compute the updated position of every point on the immersed boundary. The procedure for calculating the updated position via this method is:

$$\tilde{\boldsymbol{X}}^{n+1} = \boldsymbol{X}^n + \Delta t \boldsymbol{u}(n\Delta t, \boldsymbol{X})$$
$$\boldsymbol{X}^{n+1} = \boldsymbol{X}^n + \frac{\Delta t}{2}\Big(\boldsymbol{u}(n\Delta t, \boldsymbol{X}) + \boldsymbol{u}((n+1)\Delta t), \tilde{X}^{n+1}\Big)$$

At this point, we have the updated positions of the clot boundary. From what we discussed in Chapter 2, as the clot boundary moves all interior points move as well until they reach a new equilibrium state. Therefore, the following iterative process is performed to find the new position of each interior particle i by solving Eqn. (2.2.14).

Algorithm 2 The iterative procedure to find the equilibrium state of all interior points

1: Set $l := 1$
2: Set $\boldsymbol{Y}_0(n\Delta t, 1) :=$ the initial position of particle i
3: $\boldsymbol{Y}_0(n\Delta t, 1) :=$ the centroid of all the connected neighbors of particle i
4: Solve the Eqn. (2.2.14) with the initial value to find the updated position of $\boldsymbol{Y}(n\Delta t, 1)$
5: $l := l + 1$
6: Set $\boldsymbol{Y}_0(n\Delta t, l) = \boldsymbol{Y}(n\Delta t, l-1)$
7: Solve the Eqn. (2.2.14) with the initial value to find the updated position of $\boldsymbol{Y}(n\Delta t, l)$
8: Stop if $\|\boldsymbol{Y}(n\Delta t, l) - \boldsymbol{Y}(n\Delta t, l-1)\| < \epsilon$
9: Otherwise go to the step 6

The criterion in the step 9 means that there is no significant difference between the updated position at the current sweep and the previous on. So, we have an equilibrium state for the updated position of the interior points.

Chapter 4

SIMULATIONS AND RESULTS

In our simulations, a clot is represented as an ensemble of massless points whose boundary inside the channel is initially defined by a convex polygon the base of which lies on the lower wall of the channel.

4.0.1. Choice of parameters

The coordinates of the points on the boundary can be randomly or uniformly distributed, and clearly, the greater the number of points on the boundary, the less penetrable by the fluid it will be. The interior points are randomly selected. A Delaunay triangulation is constructed using all the points on and inside the boundary and the ones on the lower wall. The edges of the triangles in the triangulation define the initial set of springs. We follow Bajd and Serša [3] in setting the fibrin-bond spring constant κ in the Kelvin-Voigt model (2.2.14) to be equal to $0.013\,N/m$ and the viscous coefficient η to be equal to $4.6 \times 10^{-3}\,N/(m/s)$.

The non-dimensionalized fibrin-bond spring constant κ^* and viscous coefficient η^* are shown in Table 4.I and are calculated from (2.2.21) using the data in Table 2.I.

TABLE 4.I. The non-dimensionalized fibrin-bond spring constant κ^* and viscous coefficient η^* with respect to four Reynolds numbers.

Reynolds number	κ^*	η^*
444	0.0002058404×10^5	0.0074002817×10^5
360	0.000312025×10^5	0.0090992269×10^5
346	0.0003389546×10^5	0.0096200096×10^5
100	0.0040578345×10^5	0.0328571656×10^5

The general structure of the MATLAB code for calculating the fluid velocity and pressure is taken from the algorithm supplied in [40]. For computing the force exerted by the clot boundary via the immersed boundary method we use an adapted version of a two-step Peskin algorithm which

is accessible on the webpage GitHub [1]. All the computations are performed using the non-dimensionalized Navier-Stokes equations.

The number of the computational cells (see, for example, Fig. 3.8) in the x- and y- directions of the channel is taken equal to $n_x = 250$ and $n_y = 50$, respectively. The blood plasma density and viscosity are $\rho_p = 1035\, kg/m^2$ and $\eta_p = 1.4 \times 10^{-3}\, Pa.s$ [3]. The channel length and width were set equal to 5 and 1 dimensionless units, respectively. The dimensionless simulation time step equalled $\Delta t = 1 \times 10^{-3}$. The simulation results were obtained for two different multiplicative factors for the spring constant and viscous coefficient. That is to say, we changed the stiffness of the clot by multiplying κ^* and η^* by two different values.

4.1. RESULTS

4.1.1. Multiplicative factors 10^5 and 10^4

Two simulations were performed for each of the Reynolds numbers 100, 346, 360 and 444 to study the clot stability in the channnel. 100 boundary points were distributed uniformly on the boundary of a semi-ellipse for each Reynolds number in order to compare the effect of a less rigid and more rigid boundary discretization on its stability. The results of the simulations with the multiplicative factors of 10^4 and 10^5 for the spring constant and the viscous coefficient were compared by examining the screen shots of the clots' positions in the channel at a certain sequence of numbers of time steps and by calculating the average speed of the clot boundary at those times. In all the simulations the clot broke down and part of the clot detached completely as a separate ensemble (an embolus), which was then transported by the background fluid flow.

4.1.1.1. *Clot with less flexible structure - Multiplicative factor* 10^5

The following figures are the screen shots of the clot position and the average speed of the boundary points at different times for four flow regimes with the multiplicative factor set at 10^5.

The average speed and time step are dimensionless. The difference between the four flow regimes is the characteristic speed U, representing the average of the physical speed of the fully developed (Poiseuille) flow at entry. For instance,

$$U_{Re=346} = 3.46 U_{Re=100}.$$

Fig. 4.1 shows that the physical average speeds of the boundary points of the flows at Reynolds numbers 100 and 346 at dimensionless time step number 1000 are approximately equal because,

after calculating the values of the dimensionless average speeds at 1000 time steps as being approximately equal to 0.82 (for $Re = 100$) and 0.026 (for $Re = 346$), we have

$$\|\boldsymbol{u}_1\| = 0.82U_{Re=100}$$

and

$$\|\boldsymbol{u}_2\| = 0.026U_{Re=346},$$

where $\|\boldsymbol{u}_1\|_2$ and $\|\boldsymbol{u}_2\|_2$ are the average speeds at boundary points at Re=100 and Re=346, respectively. Since $U_{Re=346} = 3.46U_{Re=100}$, consequently, $\|\boldsymbol{u}_1\|_2 \approx \|\boldsymbol{u}_2\|_2$. However, t_1, the physical time corresponding to 1000 dimensionless time steps at $Re = 100$ is larger than t_2, the physical time corresponding to $Re = 346$ (in fact, $t_1 = 3.46t_2$). The conclusion is that the flow regime at the $Re = 100$ attains the same average speed as the one at the $Re = 346$, but at a later physical time. By comparing the clots' positions in Fig. 4.2 we can say that the position of the clot in the second channel (Re=346) was attained at an earlier physical time at a lower physical speed by the clot in the first channel (Re=100). Therefore, if the physical time for the second flow becomes equal to t_1, the average speed of the boundary points will be faster and the clot will be moving with a greater physical speed than the clot in the first channel.

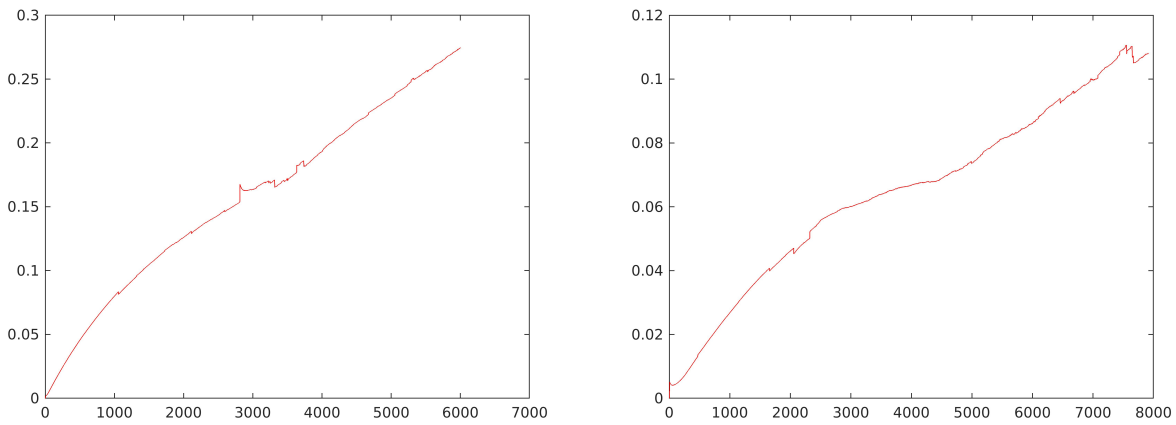

FIGURE 4.1. The average speed of the boundary points: Re=100 (left) and Re=346 (right)

Fig. 4.3 shows the clot positions at 360 and 444 after 2000 dimensionless time steps. The physical time of the snapshot in Fig. 4.2 (right) is greater than in Fig. 4.3 (left) which is greater in turn than that in Fig. 4.3 (right). The images shown in Figs. 4.4-4.14 show clot positions at $Re = 100$, 346, 360 and 444 after 4000 dimensionless time steps (Figs. 4.4-4.5), 6000 dimensionless time steps (Figs. 4.6-4.7), 7900 dimensionless time steps (Figs. 4.8-4.9), 8200 dimensionless time steps (Fig. 4.10), 8800 and 9400 dimensionless time steps (Figs. 4.11-4.13). Consider, for example, the results of the two flows given in Fig. 4.14 (right). Although the physical time in this Figure after 6000 dimensionless time steps is comparable to the physical time in Fig. 4.1 (right) after 7900

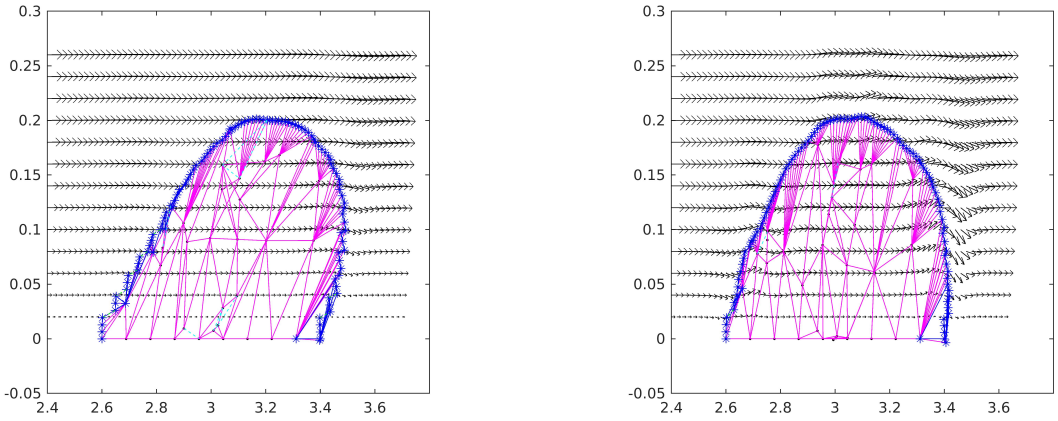

FIGURE 4.2. Clot position after 2000 time steps for Re=100 (left) and Re=346 (right)

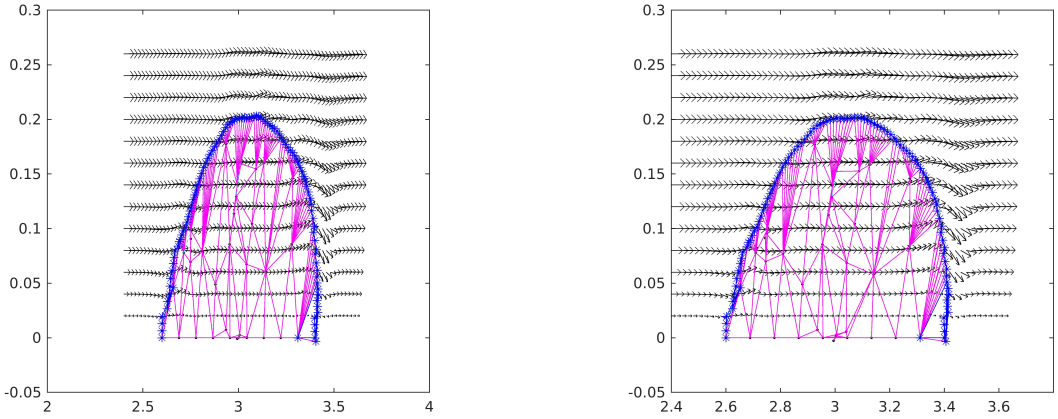

FIGURE 4.3. Clot position after 2000 time steps for Re=360 (left) and Re=444 (right)

dimensionless time steps, the physical average speed at $Re = 444$ is larger than that at $Re = 3600$, as one would expect.

At $Re = 100$, Fig. 4.6 (left) indicates that the clot has broken down into smaller ensembles. The average speed increases steadily. There are two peaks at around dimensionless time steps 2800 and 3700 (see Fig. 4.1 (left)). The former indicates that the bonds between the boundary points were still intact but thereafter the tensions and extensions became so high that these bonds snapped. Some interior points became new boundary points and the whole clot recovered shortly. The average speed of the boundary points was changing very slowly up to around 3300 time steps, which was showing a more or less stable clot. Thereafter, the average speed started increasing steadily again and they were still intact. We conjecture that at around dimensionless time step 3700 the tensions and extensions of the bonds between the boundary points again became so high that they snapped which led to a detachment from the main clot, i.e. a secondary clot (an embolus), a sudden movement of some boundary points on the main clot back to regions of lower fluid speed

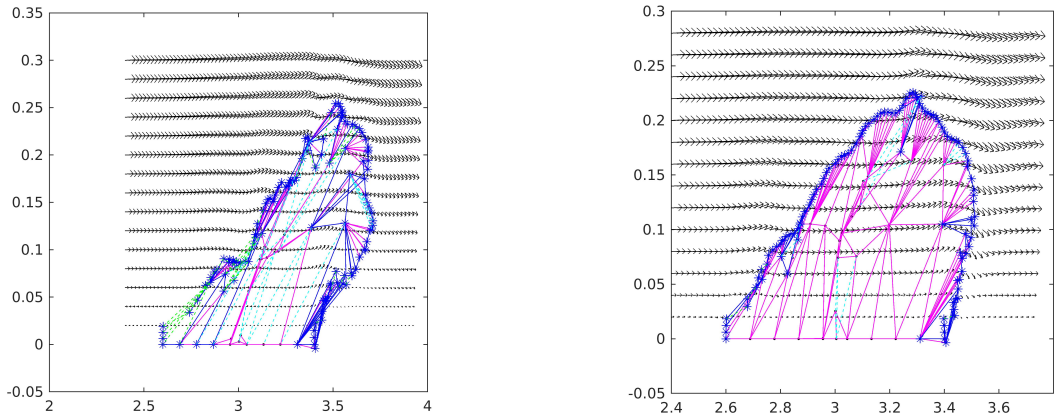

FIGURE 4.4. Clot position after 4000 time steps for Re=100 (left) and Re=346 (right)

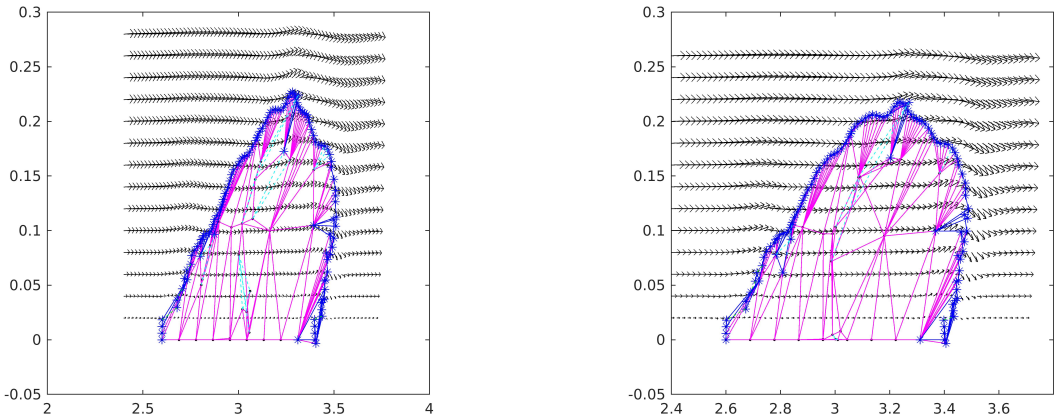

FIGURE 4.5. Clot position after 4000 time steps for Re=360 (left) and Re=444 (right)

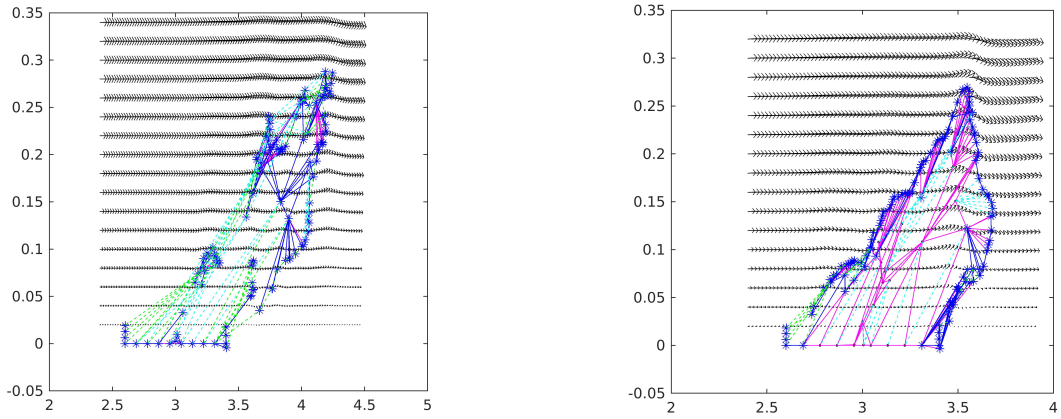

FIGURE 4.6. Clot position after 6000 time steps for Re=100 (left) and Re=346 (right)

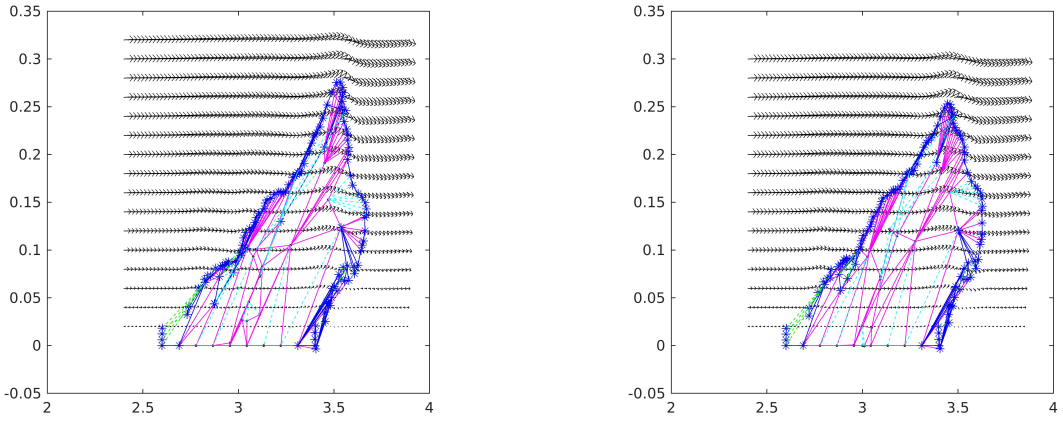

FIGURE 4.7. Clot position after 6000 time steps for Re=360 (left) and Re=444 (right)

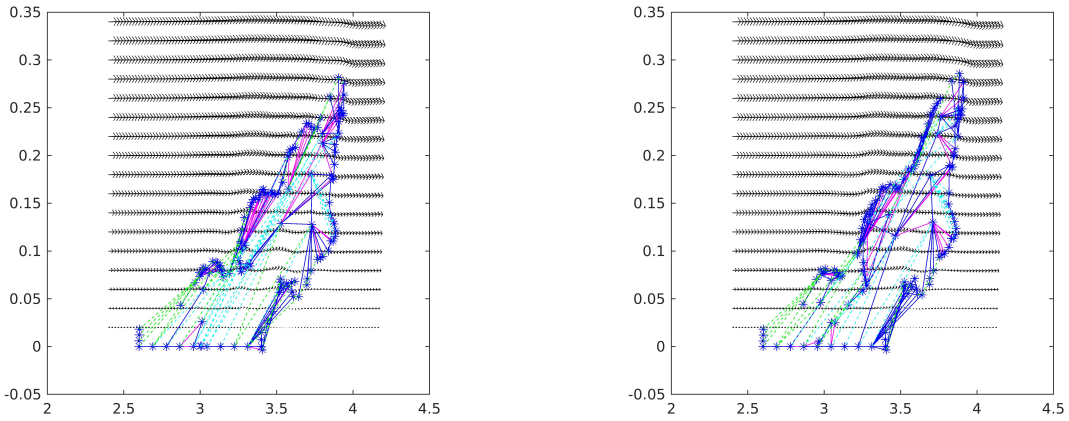

FIGURE 4.8. Clot position after 7900 time steps for Re=346 (left) and Re=360 (right)

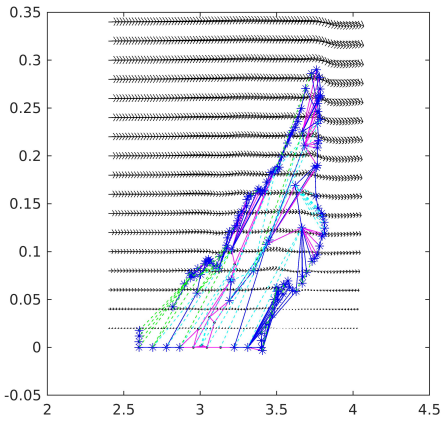

FIGURE 4.9. Clot position after 7900 time steps for Re=444

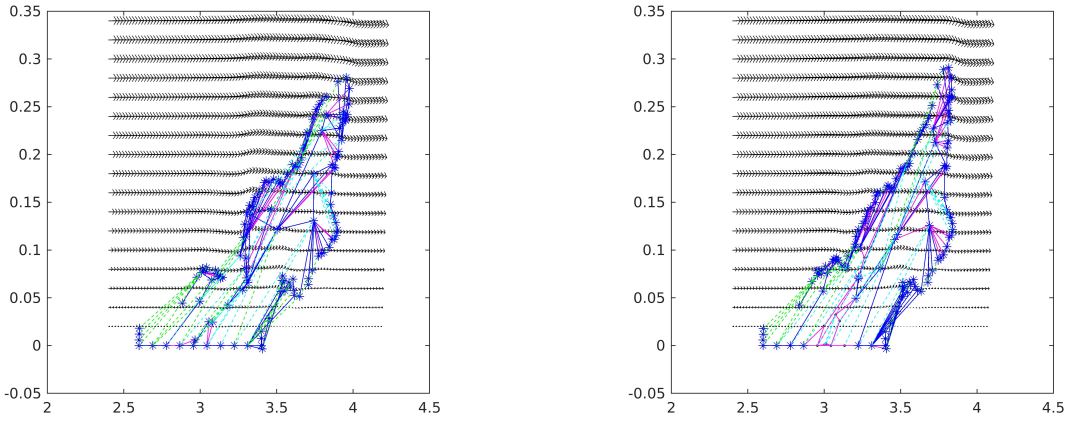

FIGURE 4.10. Clot position after 8200 time steps for Re=360 (left) and Re=444 (right)

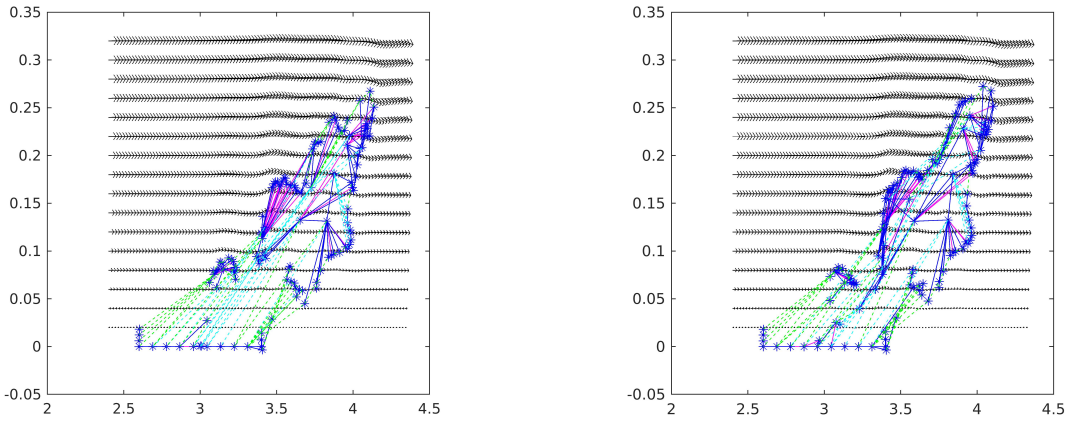

FIGURE 4.11. Clot position after 8800 time steps for Re=346 (left) and Re=360 (right)

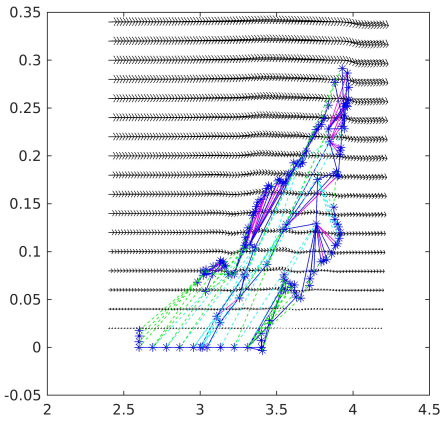

FIGURE 4.12. Clot position after 8800 time steps for Re=444

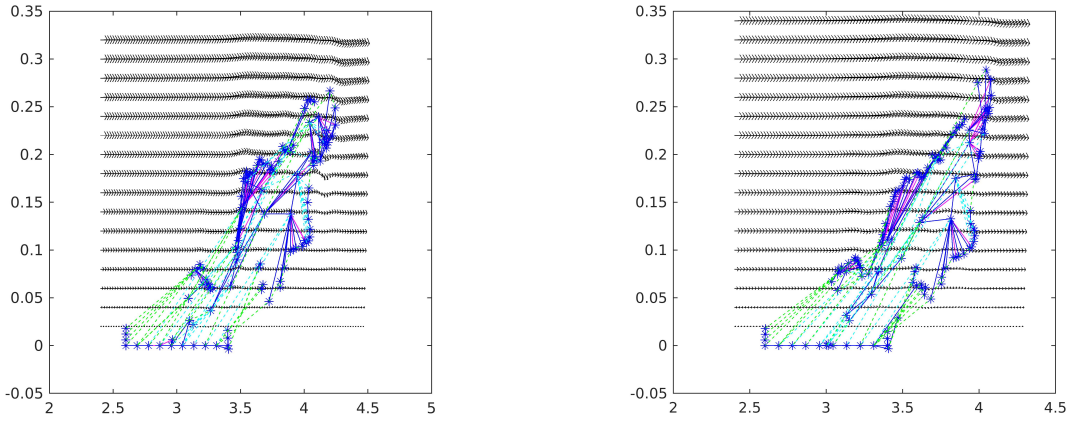

FIGURE 4.13. Clot position after 9400 time steps for Re=360 (left) and Re=444 (right)

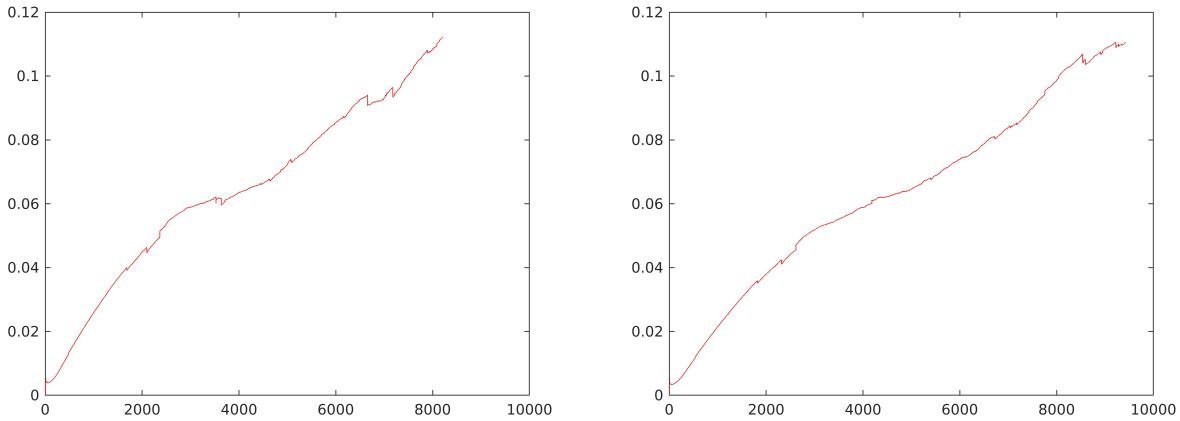

FIGURE 4.14. The average speed of the boundary points: Re=360 (left) and Re=444 (right)

and movement of the embolus away from the main clot. We observe that although the average speed drops following the snapping of bonds and the release of an embolus, it recovers shortly thereafter.

Note that the interpretation of the results for the Reynolds numbers of 346, 360 and 444 was complicated by the fact that to change the Reynolds number we should have used different characteristic average speeds *and* slightly different characteristic lengths, in order to keep these quantities in the physiological realm. Therefore, to avoid such a complicated situation, we fixed the quantity of the characteristic length. Consequently, for obtaining these Reynolds numbers, we only changed the characteristic average speeds.

However, the clot has broken down in both cases corresponding to $Re = 346$ and $Re = 444$, see Fig. 4.13.

Finally, since the characteristic speed of the flow at Reynolds number 360 is smaller than the one at Reynolds number 444, the clot's state for the latter is shown at an earlier physical time in Fig. 4.13. Therefore, when the physical time for the latter gets to the current physical time of the former, the clot may be expected to break down and for there to be at least two separate ensembles, which is confirmed by the result shown in Fig. 4.13 (right).

4.1.1.2. *Clot with more flexible structure - Multiplicative factor* 10^4

Another set of simulations with a smaller multiplicative factor (10^4) of the spring constant and the viscous coefficient was executed to study the effect of the change of rigidity of the clot on its motion.

What we expected was that the less rigid clot would be less resistant and move faster, which would lead to more snapped bonds at an earlier time (both dimensionless and physical) in comparison to the more rigid one, i.e. the clot with a multiplicative factor (10^5) of the spring and viscous coefficient. By comparing the results in Figs. 4.15-4.22 with those in Figs. 4.2-4.10, we observe that the bonds in the more flexible clot snapped faster than those in the more rigid clot. The comparison of the results of the average speed of the boundary points in Figs. 4.23 and 4.24 with the ones in Figs. 4.1 and 4.14 confirm that the smaller the multiplicative factor of the spring and viscous coefficient is, the faster the clot moves.

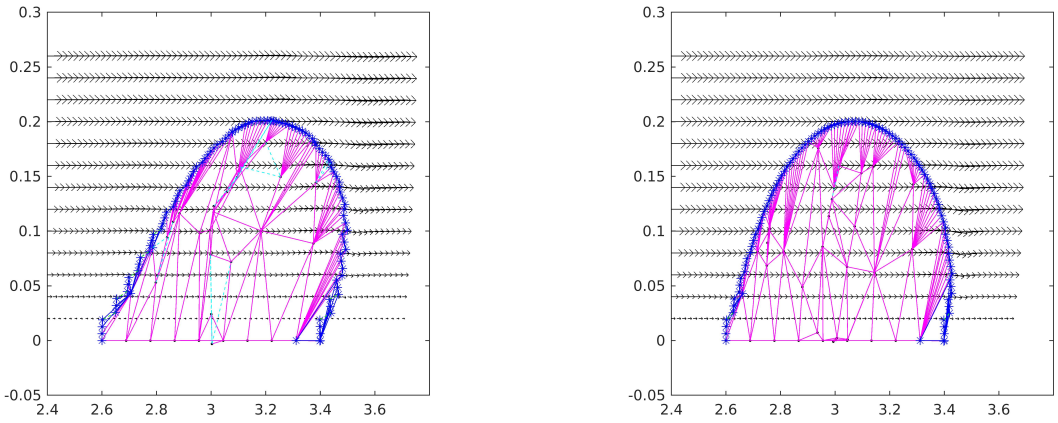

FIGURE 4.15. Clot position after 2000 time steps for Re=100 (left) and Re=346 (right)

In Figs. 4.17-4.22 we observe the displacement of the clot, its resistance against the flow and how fast it breaks down into smaller secondary clots (emboli) at different Reynolds numbers. The majority of the snapshots are taken at the same number of dimensionless time steps as in Section 4.1.1.1 for the purpose of being comparable with the results obtained with the larger multiplicative factor.

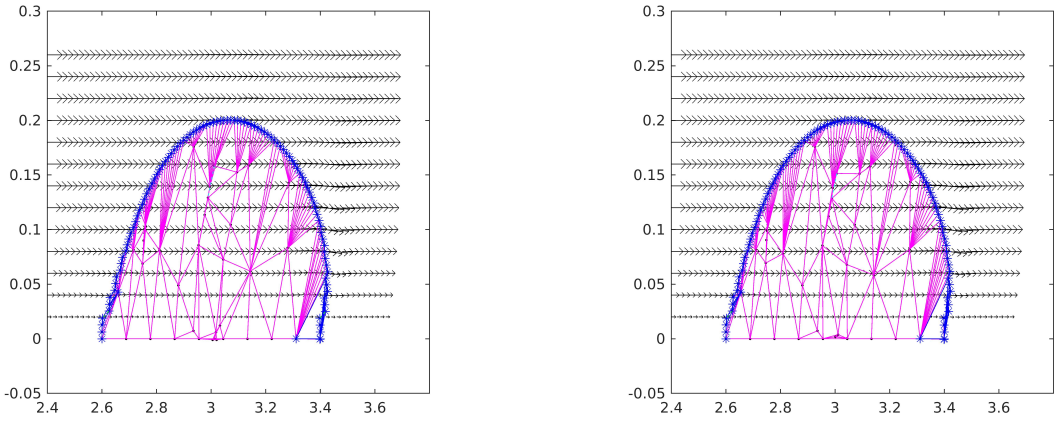

FIGURE 4.16. Clot position after 2000 time steps for Re=360 (left) and Re=444 (right)

Some of the snapshots were taken at an earlier dimensionless time steps due to the fact that the clot had broken down already into smaller ensembles. Therefore, it was pointless letting the simulation keep running.

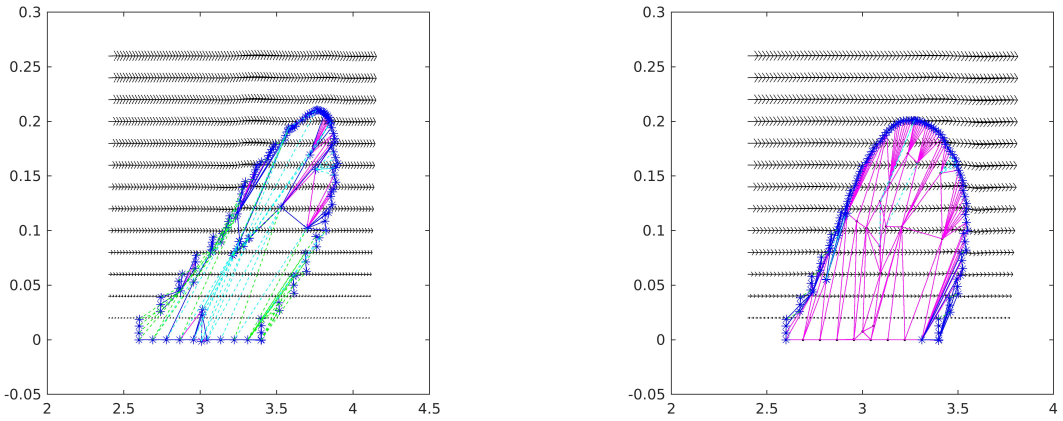

FIGURE 4.17. Clot position after 4000 time steps for Re=100 (left) and Re=346 (right)

All the results are compatible with our assumption that the possibility of having a steady state for a more flexible clot is less likely. For example, comparing the results in Figs. 4.22 (right) and 4.10 (right) demonstrates that the more flexible clot in the former has been already broken down into smaller ensembles while in the latter the main body is still intact and attached to the lower wall although the tensions are so high that in a later time those bonds snapped.

Finally, the following figures show the average speed of the boundary points for Reynolds numbers 100 (Fig. 4.23 (left)), 346 (Fig. 4.23 (right)), 360 (Fig. 4.24 (left)) and 444 (Fig. 4.24 (right)).

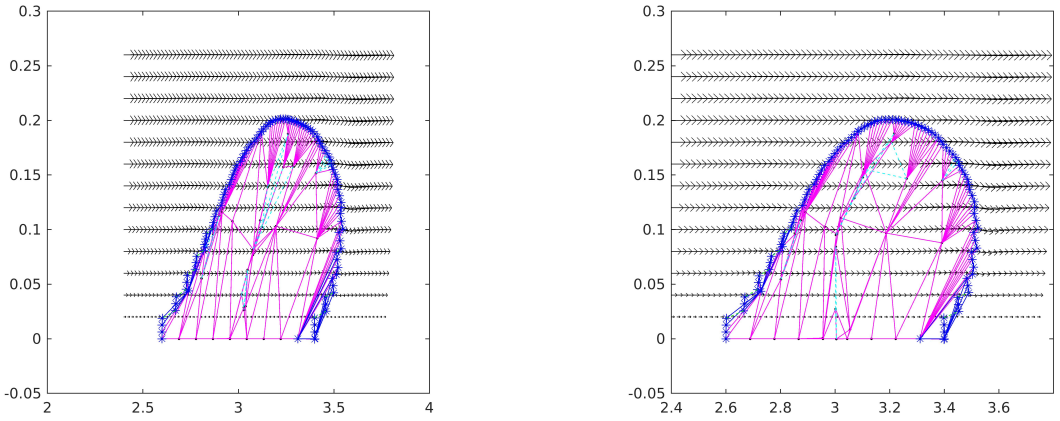

FIGURE 4.18. Clot position after 4000 time steps for Re=360 (left) and Re=444 (right)

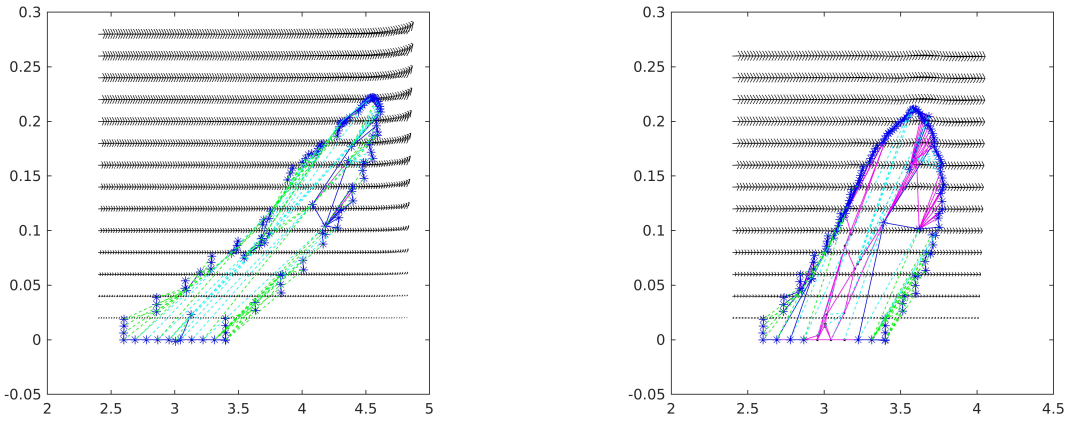

FIGURE 4.19. Clot position after 6000 time steps for Re=100 (left) and Re=346 (right)

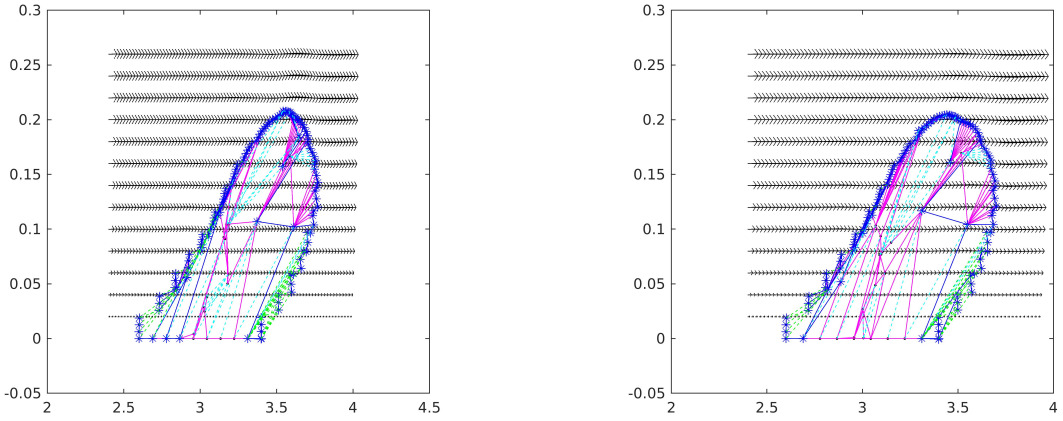

FIGURE 4.20. Clot position after 6000 time steps for Re=360 (left) and Re=444 (right)

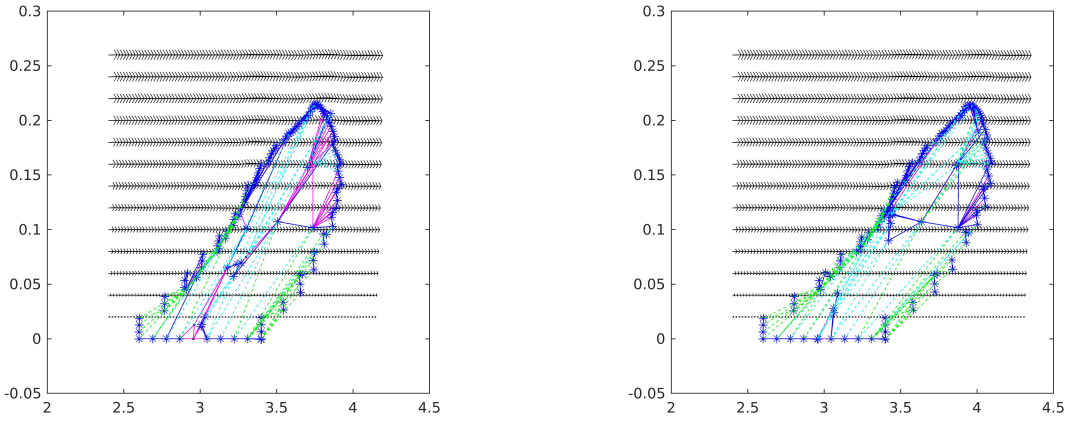

FIGURE 4.21. Clot position after 7900 time steps for Re=346 (left) and Re=360 (right)

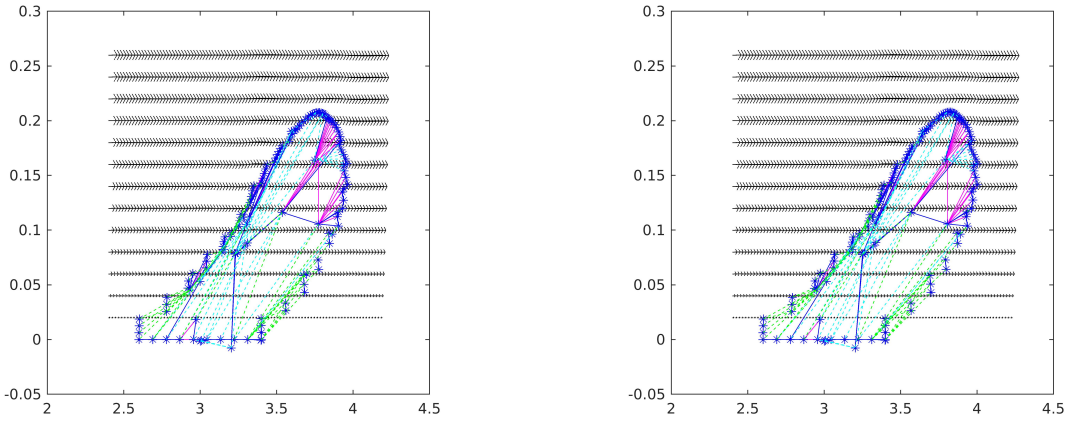

FIGURE 4.22. Clot position after 7900 (left) and 8200 (right) time steps for Re=444

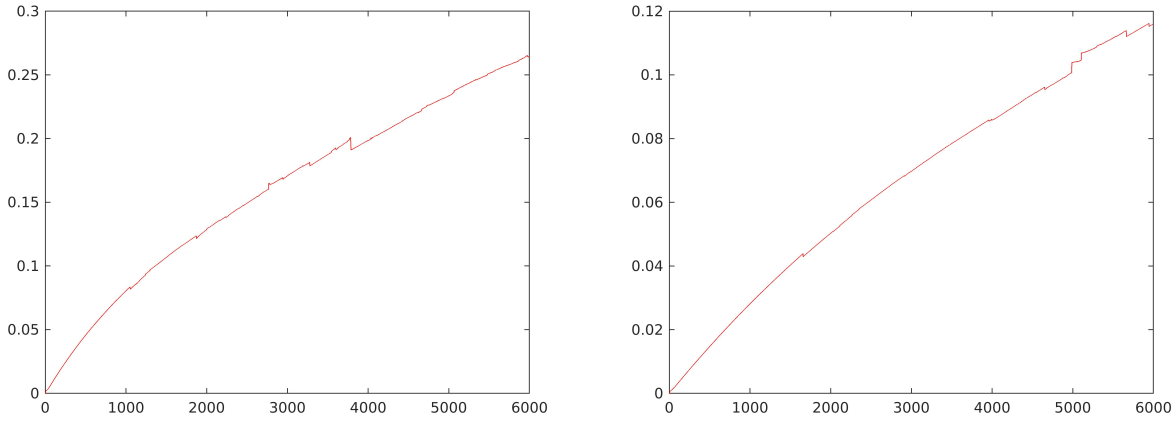

FIGURE 4.23. The average speed of the boundary points for Re=100 over 6000 time steps (left) and Re=346 over 7900 time steps (right)

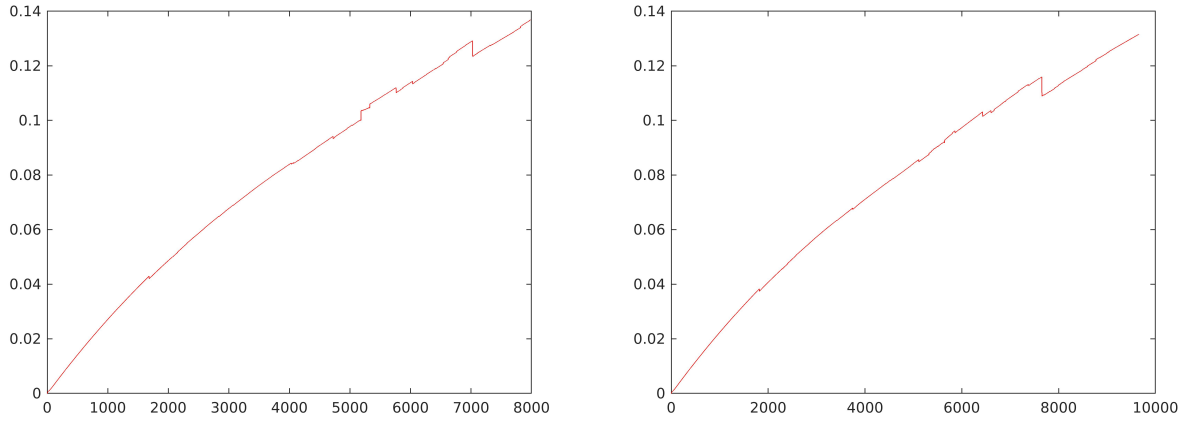

FIGURE 4.24. The average speed of the boundary points for Re=360 over 7900 time steps (left) and Re=444 over 8200 time steps (right)

As we see, the multiplicative factor of 10^4 corresponds to bonds that are less stiff than those in Section 4.1.1.1. Therefore, less resistance is observed in clot displacement. All flow regimes bring about clot break-down and partial detachment from the lower wall. Again, dimensionless time steps are not the same as the physical time steps. In other words, by fixing a number of dimensionless time steps at two different Reynolds numbers, the corresponding physical times are not the same. Moreover, the average speed of the boundary points is dimensionless too. All the interpretations given for the multiplicative factor 10^5 are valid here. The only difference is that by keeping all the other conditions and parameters the same, the less stiff clot (with multiplicative factor 10^4) moves faster than the stiffer clot (with multiplicative factor 10^5).

4.2. CONCLUSIONS

In this thesis, we have studied the behavior of two different idealized clots under different two-dimensional blood flow regimes. For each type of clot we performed numerical simulations at Reynolds numbers of 100, 346, 360 and 444. We tested several solvers available in MATLAB to solve the nonlinear equations for finding the equilibrium positions of interior points at each time step and arising from use of the Kelvin-Voigt spring model. The positions of the boundary particles of the clot were determined from use of the immersed boundary method. The Kelvin-Voigt model used in this work is a revised and corrected version of a model described by Bajd and Serša [3].

In none of the cases studied were we successful in getting a stationary solution for the boundary particle positions which has been, admittedly, both a surprise and a disappointment. The choice of Reynolds numbers made in this thesis led not only to the bonds between particles snapping, but also to the creation of emboli. Even in flows at much smaller Reynolds numbers the clot would

fragment into pieces which could result in embolism, although, of course, this process would take much longer than at higher values of Re.

BIBLIOGRAPHY

[1] https://github.com/eldila/MatIB/tree/master, 2013.

[2] S. Appiah, I. Adentunde, and I. Dontwi. Mathematical model of blood clot in the human cardiovascular system. *Int. J. Res. Biochem. Biophys.*, 1(2):9–17, 2011.

[3] F. Bajd and I. Sersa. Mathematical modeling of blood clot fragmentation during flow-mediated thrombolysis. *Biophys. J.*, 104(5):1181–1190, 2013.

[4] R. P. Beyer and R. J. Leveque. Analysis of one-dimensional model for the immersed boundary method. *SIAM. J. Numer. Anal.*, 29(2):332–364, 1992.

[5] T. Bodnar and A. Sequeira. Numerical simulation of the coagulation dynamics of blood. *Comput Math. Methods in Medicine*, 9(2):83–104, 2008.

[6] D. L Brown, R. Cortez, and M. L. Minion. Accurate projection methods for the incompressible Navier-Stokes equations. *J. Comput. Phys.*, 168(2):464–499, 2001.

[7] A. J. Chorin. Numerical solution of the Navier-Stokes equations. *Math. Comp.*, 22(104):745–762, 1968.

[8] A. J. Chorin. On the convergence of dicrete approximation to the Navier-Stokes. *Math. Comput.*, 23(106):341–353, 1969.

[9] J. Collet, H. Shuman, R. Ledger, S. Lee, and J. Weisel. The elasticity of an individual fibrin fiber in a clot. *PNAS*, 102(26):9133–9137, 2005.

[10] A. J. Comerota. Thrombolysis for deep venous thrombosis. *J. Vasc. Surg.*, 55(2):607–611, 2012.

[11] D. Devendran and E. Corona. Computational fluid dynamic group: Projection methods. http://cims.nyu.edu/~kellen/cfd/CFD_Reading_Projection_Methods_Notes.pdf, NYU, 2009.

[12] R. Douma and H. Buller. Acute pulmonary embolism. Part 2: treatment. *Nat. Rev. Cardiol.*, 7(11):613–622, 2010.

[13] A. Fogelson. A mathematical model and numerical method for studying platelet adhesion and aggregation during blood clotting. *J. Comput. Phys.*, 56(1):111–134, 1984.

[14] A. Fogelson. Continuum models of platelet aggregation: Formulation and mechanical properties. *SIAM J. Appl. Math.*, 52(4):1089–1110, 1992.

[15] A. Fogelson. Cell-based models of blood clotting. In *Single-Cell-Based Models in Biology and Medicine*. 243-269, Birkhäuser Verlag, Basel, 2007.

[16] A. Fogelson. An introduction to the mathematical modeling of blood clotting. https://www.ima.umn.edu/materials/2010-2011/SW9.13-15.10/10070/ima2010.pdf, University of Utah, 2012.

[17] A. Fogelson. Fogelson's coagulation model notes. http://www.math.utah.edu/~fogelson/6780_s13/kuhfogmodelextended.pdf, University of Utah, 2013.

[18] A. Fogelson and N. Tania. Coagulation under Flow: the influence of flow-mediated transport on the initiation an inhibition of coagulation. *Pathophysiol. Haemost. Thromb.*, 34(2-3):91–108, 2005.

[19] G. Strang. *Computational Science and Engineering*. Wellesely Cambridge Press, Wellesely, 2007.

[20] J. L. Guermond, P. Minev, and J. Shen. An overview of projection methods for incompressible flows. *Comput. Methods Appl. Mech. Eng.*, 195(44-47):6011–6045, 2006.

[21] M. Khanin, V. Leytin, and A. Popov. A mathematical model of kinetics of platelets and plasma hemostasis system interaction. *Thromb. Res.*, 64(6):659–666, 1991.

[22] M. Khanin, D. Rakov, and A. Kogan. Mathematical model for the blood coagulation prothrombin time test. *Thromb. Res.*, 89(5):227–232, 1998.

[23] M. Khanin and V. Semenov. A mathematical model of the kinetics of blood coagulation. *J. Theor. Biol.*, 136(2):127–134, 1989.

[24] E. Khramchenkov and M. Khramchenkov. Mathematical modeling of the lysis of clots in blood vessels. *J. Eng. Phys. Thermophys.*, 84(5):1026–1033, 2011.

[25] M. C. Lai and C. S. Peskin. An immersed boundary method with formal second-order accuracy and reduced numerical viscosity. *J. Comput. Phys.*, 160(2):705–719, 2000.

[26] S. N. Levin. Enzyme amplifier kinetics. *Science*, 152(3722):651–653, 1966.

[27] J. S. Milner, J. A. Moore, B. K. Rutt, and D. A. Steinman. Hemodynamics of human carotid artey bifurcations: Computational studies with models reconstructed from magnetic resonance imaging of normal subjects. *J. Vasc. Surg.*, 28(1):143–156, 1998.

[28] R. Mittal and G. Iaccarino. Immersed boundary methods. *Annu. Rev. Fluid Mech. J.*, 37:239–261, 2005.

[29] D. Mori, K. Yano, K. Tsubota, T. Ishikawa, S. Wada, and T. Yamaguchi. Simulation of platelet adhesion and aggregation regulated by fibrinogen and von Willebrand factor. *Thromb. Haemost.*, 99(1):108–115, 2008.

[30] N. Özkaya and Dawn Leger and David Golsheyder and Margareta Nordin. *Fundamentals of biomechanics: Equilibrium, motion, and deformation*. Springer Science+Business Media, New York, 2012.

[31] C.W. Oosterle, H. Bijil, H.X. Lin, S.W. de Leeuw, J.B. Perot, C. Vuik, and P. Wesseling. Fast solution methods and parallelization for computational science applications, Lecture notes for course (wi4145TU) "Computational science and engineering". http://citeseerx.ist.psu.edu/viewdoc/download?doi=10.1.1.110.78&rep=rep1&type=pdf, TUDelft.

[32] K. Ouriel, F. J. Veith, and A. A. Sasahara. Thrombolysis or peripheral arterial surgery (TOPAS) investigators; A comparison of recombinant urkinase with vascular surgery as initial treatment for acute arterial occlusion of the legs. *N. Engl. J. Med.*, 338(16):1105–1111, 1998.

[33] R. G. Owens and T. N. Phillips. *Computational Rheology*. Imperial College Press, London, 2002.

[34] C. S. Peskin. Flow patterns around heart valves: A numerical method. *J. Comput. Phys.*, 10(2):252–271, 1972.

[35] C. S. Peskin. Numerical analysis of blood flow in the heart. *J. Comput. Phys.*, 25(3):220–252, 1977.

[36] C. S. Peskin. The immersed boundary method. *Acta Numerica*, pages 479–517, 2002.

[37] B. Pohls, C. Beringer, M. Bomhard, and F. Keller. The quick machine – A mathematical model for extrinsic activation of coagulation. *Haemostasis*, 24(6):325–337, 1994.

[38] A. M. Roma, C. S. Peskin, and M. J. Berger. An adaptive version of the immersed boundary method. *J. Comput. Phys.*, 153(2):509–534, 1999.

[39] E. M. Saiki and S. Biringen. Numerical simulation of a cylinder in uniform flow: Application of a virtual boundary method. *J. Comput. Phys.*, 123(2):450–465, 1996.

[40] B. Seibold. A compact and fast Matlab code solving the incompressible Navier-Stokes equations on rectangular domains. http://math.mit.edu/~gs/cse/codes/mit18086_navierstokes.pdf, MIT, 2008.

[41] L. Sekoranja, J. Loulidi, and R. Sztajzel. Intravenous versus combined (intravenous and intra-arterial) thrombolysis in acute ischemic stroke: a transcranial color-coded duplex sonography-guided pilot study. *Stroke*, 37(7):1805–1809, 2006.

[42] V. Semenov and M. Khanin. Nonlinear effects in kinetics of blood coagulation. *Biofizika*, 35(1):139–141, 1990.

[43] E. Shavlyugin, L. Hanin, and M. Khanin. Dynamics of pathologic clot formation: a mathematical model. *J. Theor. Biol*, 340:96–104, 2014.

[44] A. Tokarov, I. Sirakov, G. Panasenkov, E. Shnol V. Volpert, A. Butylin, and F. Ataullakhanov. Continuous mathematical model of platelet thrombus formation in blood flow. *Russ J. Anal. Math. Modell.*, 27(2):191–212, 2012.

[45] C. Tu and C. S. Peskin. Stability and instability in the computation of flows with moving immersed boundaries: A comparison of three methods. *SIAM J. Sci. and Statist. Comput*, 13(6):1361–1376, 1992.

[46] N. Wang and A. Fogelson. Computational methods for continuum models of platelet aggregation. *J. Comput. Phys.*, 151(2):649–675, 1999.

[47] G. Williems, T. Lindohout, W. Hermens, and H. Hemker. Simulation models for thrombin generation in plasma. *Haemostasis*, 21(4):191–207, 1991.